

NORTHWESTERN UNIVERSITY

Mapping Galactic Clouds with the Balloon-Borne Large Aperture
Submillimeter Telescope (BLAST)

A DISSERTATION

SUBMITTED TO THE GRADUATE SCHOOL
IN PARTIAL FULFILLMENT OF THE REQUIREMENTS

for the degree

DOCTOR OF PHILOSOPHY

Field of Physics and Astronomy

By

Paul A. Williams

EVANSTON, ILLINOIS

December 2021

© Copyright by Paul A. Williams 2021

All Rights Reserved

ABSTRACT

Mapping Galactic Clouds with the Balloon-Borne Large Aperture Submillimeter
Telescope (BLAST)

Paul A. Williams

One of the most pressing open questions in star formation is the role of magnetic fields relative to turbulence and gravity, and how these three processes set the stellar initial mass function and star formation efficiency. In this work, we present the state of BLAST-TNG (the Balloon-borne Large Aperture Submillimeter Telescope - The Next Generation) a polarimeter built to measure magnetic fields in molecular clouds, and new results obtained by comparing polarimetric observations from BLASTPol (The Balloon-borne Large Aperture Submillimeter Telescope for Polarimetry), PolKa (English name: Polarimeter for bolometer cameras), and ALMA (Atacama Large Millimeter/submillimeter Array).

The role of magnetic fields in star formation remains an open question because magnetic field strength is difficult to measure directly. Measurements of Zeeman splitting are the only method to measure magnetic field strength directly in molecular clouds, but these measurements are very difficult to make and have yielded only a few tens of detections (Crutcher, 2012). Indirect measurements, which only measure magnetic field direction,

are significantly simpler. These measurements have been made for entire molecular clouds at moderate resolution (Fissel et al., 2016), and for the entire sky at low resolution by *Planck* (Lamarre et al., 2010; Planck Collaboration et al., 2014, 2015).

Magnetic field direction can be mapped using dust emission polarimetry. Aspherical dust grains in the interstellar medium tend to align with their long axes perpendicular to the magnetic field, and emit light that is polarized along their long axis. Therefore, to measure magnetic field direction, we can rotate measured polarization vectors by 90° . These dust grains are cold (15-50 K), therefore this emission peaks in the submillimeter.

The BLAST Collaboration has built several instruments over the past two decades, two of which (BLASTPol, Galitzki et al. (2014) and BLAST-TNG, Lourie et al. (2018a)) were polarimeters built to study the role of magnetic fields in star formation. This work describes the flight history of the BLAST instruments, the technological advancements that made BLAST-TNG possible, the pointing system (of which key components were developed at Northwestern), and several analyses completed after the flight.

We also describe some recent work which compares magnetic field measurements across three orders of magnitude in spatial scale, which required observations from BLASTPol, PolKa, and ALMA. We find that the densest part of Vela C South Ridge contains a star forming core threaded by magnetic fields that have a consistent direction across all spatial scales measured. This indicates that the magnetic field has energy density at least as great as that in turbulent gas motion (Ostriker et al., 2001).

Acknowledgements

First, I would like to thank Giles for everything he has done as my advisor. It is difficult to overstate the impact advisors have on their students, and I don't think I could have had a better one. He always gave me good guidance for the work I was doing, and was understanding and supportive about personal matters.

To everyone on BLAST, but especially to Laura, Federico, and Peter for mentoring me as I learned all about the instrument, the software, valves, electronics, stepper motors, and so much more. To the entire team that deployed to the ice including: Ian, Nate, Adrian, Sam, Javier, Gabriele, Caleb, Nick, Mark, and Phil; for all the hikes, meals in the LDB galley, movie nights in 207, and evenings in the music room. All of these made being in McMurdo feel so much more like home.

To the entire team at CSBF, the success of BLAST-TNG would have been impossible without you. Thank you for helping us with every lift, cryogen fill, and especially, all eleven launch attempts. It was great getting to know you all over the six months we spent together in Palestine and McMurdo.

To all my friends who supported me all these years, but especially the following. Mark, for so consistently having lunch with me every week, even (and especially) while we have worked remotely due to COVID. Rachel, for always texting when I forgot and making sure we found time to talk. Kristine and Michael, for all the dinners, walks to the Point, and

board game nights. Barb, for welcoming the research group into her home and supporting Morgane while I was in Antarctica.

Finally, I would never have finished this PhD without the support and love of my family. I would especially like to thank my wife, Morgane¹, my parents, David and Mary, and my brothers, Joseph, David, and Michael for all their understanding and support over these six years, especially while I was in Antarctica launching BLAST-TNG for two consecutive holiday seasons. Those months were particularly hard on Morgane and many of our friends, especially those in Chicago, supported her through them.

¹Additional thanks to Morgane for proof-reading this dissertation!

Table of Contents

ABSTRACT	3
Acknowledgements	5
Table of Contents	7
List of Tables	9
List of Figures	10
Chapter 1. Introduction	19
1.1. Magnetic Fields and Star Formation	19
1.2. BLAST	20
1.3. Linking Magnetic Fields Across Spatial Scales	27
1.4. Stokes Parameters and Instrumental Polarization	30
1.5. Outline	32
Chapter 2. BLAST-TNG Pointing System	34
2.1. Pointing Motors	34
2.2. Pointing Sensors	34
2.3. Pointing Control	40
2.4. Pinhole Sun Sensor Design and Construction	43

Chapter 3. BLAST-TNG 2020 Flight Pointing Data Analysis	49
3.1. Differential GPS Calibration	49
3.2. Pinhole Sun Sensor Calibration	51
3.3. Finding Home	61
Chapter 4. PolKa Data Analysis	67
Chapter 5. Magnetic Field Measurements in Vela C South Ridge	81
5.1. Previous Work	81
5.2. Observations	84
5.3. Magnetic Field Morphology Across Spatial Scales	85
5.4. Magnetic Field Direction Consistency	86
5.5. Discussion	88
Chapter 6. Conclusion	91
6.1. Importance of Star Formation	91
6.2. BLAST-TNG	91
6.3. Vela C South Ridge Magnetic Field Measurements	92
6.4. Future Work	93
References	95

List of Tables

2.1	Star Camera Properties: The two star cameras flown on BLAST-TNG were identical and were both mounted parallel to the boresight of the telescope.	35
2.2	Star Camera Performance: The total images solved during and after the flight, using STARS (Chapman et al., 2014) during the flight and software from astrometry.net (Lang et al., 2010) post-flight.	36
2.3	Pointing Sensor Properties	38
2.4	Specifications for the final two ADCs we considered for the Pinhole Sun Sensors. The two blank cells for the Storage Temperature and Weight of the Labjack T7 are specifications that we were unable to find prior to deciding which to buy. The quotes given are from late 2015.	45
3.1	The 14 calibration parameters for the simultaneous fit of all 4 PSSs and both star cameras (XSC = star camera). Equation 3.6 was used for this fit.	56
3.2	The star camera pointing offsets found from comparing our maps of East Home to those from <i>Herschel</i> .	63

List of Figures

- 1.1 BLAST-TNG on the flightline with the balloon almost entirely inflated. The balloon is visible on the left, with the launch vehicle and BLAST-TNG on the far right. This picture was taken a few minutes before launch. 22
- 1.2 Front view of BLAST-TNG with major systems labeled. The primary and secondary mirror are both mounted on the inner frame, which can move in elevation (driven by the elevation motor). The pivot motor and reaction wheel rotate the entire gondola in azimuth. See Figure 1.3 for a side view. Three of the antennas we use to communicate with the payload during flight are visible on the top of the gondola. The solar panel arrays, which power the instrument in flight, are folded close to the gondola in this configuration. Before launch they are unfolded so they face 110° to the right of the front of the telescope. 24
- 1.3 Side view (port) of BLAST-TNG with major systems labeled. The star cameras, cryostat, and carbon fiber sun shield, together with the primary and secondary mirrors (shown in Figure 1.2), are all mounted on the inner frame, which moves in elevation (driven by the elevation motor). The sun shield mounted on the back and sides of the gondola

is covered in aluminized mylar on the back and starboard side because we keep those sides facing the sun during flight. The highbay is the building with the large open doors on the left. The black structure in the upper right that the instrument is suspended from is part of the launch vehicle.

25

1.4 Diagram depicting the basic MKID polarimeter design consisting of two detectors, each sensitive to one of two orthogonal linear polarizations. The capacitors are labeled as “IDCs” in this figure, which stands for inter-digitated capacitor, a type of capacitor with inter-laced digits, like those shown in this figure.

27

1.5 This shows the overlap in spatial scales for the BLASTPol, PolKa, and ALMA magnetic field measurements. The top left panel shows BLASTPol 500 μm Stokes I (in instrument units) with BLASTPol inferred magnetic field direction in white vectors. The top right panel shows LABOCA 870 μm Stokes I (Jy/beam) with PolKa inferred field direction in magenta, and BLASTPol in white. The bottom panel shows ALMA 2 mm Stokes I (Jy/beam) with ALMA inferred field in black, and PolKa in magenta. The top right image is about 12 pc across, the top left is 1 pc, and the bottom image is about 0.1 pc across.

29

1.6 Depiction of the polarization of light corresponding to the three polarized Stokes parameters (Q , U , V). In each case, the red line or circle indicates the path traced by the tip of the electric field vector, viewed from the point of view of the source (the convention for circular

polarization used in radio astronomy). Image credit: Dan Moulton, used under the terms of CC BY-SA 3.0.

32

- 2.1 Example star camera images showing polar mesospheric clouds (PMCs) with various brightnesses. All images have an inverted scale, with bright pixels represented by black and dark pixels represented by white. 37
- 2.2 Example of an az-el go to command showing the pointing stability of BLAST-TNG. In this example, stability is 2.4'' in az and 7.1'' in el. This is calculated from the standard deviation in az and el over ten minutes, during the period shown in Figures 2.2b and 2.2d. The horizontal axes in all 4 plots are in seconds, and the vertical axes are in degrees. 42
- 2.3 The enclosure for the PSS Labjack T7 in an early stage of development. The T7 is the large printed circuit board in the lower right of the image. The small black and silver electrical components in the center are the DC/DC converter and micro ripple attenuator modules, which we use to convert and condition the 24 V battery power available on the gondola to 5 V for use by the T7. This version of the T7 box did not use the Mux80 multiplexer board, which plugs into the T7 at the DB37 connector on the upper right of the PCB. In the flight version, the T7 was connected to the gondola network via ethernet. 46
- 2.4 PSS testing and calibration setup in Dearborn Observatory. 48

- 3.1 Histogram showing the difference between the DGPS and Star Camera 0 (XSC0) azimuth pointing solutions, in degrees. This is based on 236 solutions from XSC0. 51
- 3.2 Histogram of the residuals of PSS global fit. The 14 parameter fit predicts the difference between PSS and star camera az solutions with an RMS error of 0.19° . 57
- 3.3 The calibrated PSS solutions for the entire flight of BLAST-TNG. Each PSS is shown in its own color, individual solutions are dots, but they mostly blend together at this scale. Each PSS covers a different range of azimuth, which is fixed relative to the sun, but decreases in time (because the sun's azimuth decreases during the day due to the rotation of the Earth). The only two sun sensors which have overlapping fields-of-view are PSS3 and PSS4, which can be seen from this plot by the fact that the green and orange points overlap in several time ranges. At the beginning of the range shown the balloon and telescope were ascending and the telescope was rotating freely through 360° of azimuth, which is why all 4 sun sensors viewed the sun during that time. Expanding the time axis shows that each PSS viewed the sun at separate times, with the exception of PSS3 and PSS4 on the edges of their fields-of-view. 58
- 3.4 The calibrated azimuth solution for PSS4 during a scan of a target. As discussed in Section 2.3, during most target scans we scan slowly in

elevation while scanning more quickly in azimuth, which can be seen in this figure. 59

3.5 Differences between the calibrated azimuth solutions for PSS4 and PSS3, during times when the sun was in the fields-of-view of both sun sensors. 60

3.6 A *Planck* 350 μm map of the “Home” source and several sources around it. The colorscale shows specific intensity in units of MJy/sr and the coordinate grid is in right ascension (or RA, horizontal) and declination (or Dec, vertical). 62

3.7 BLAST-TNG single detector map of East Home (RCW 92B) with a black line drawn between the two compact sources. The linear object at the bottom of the map is an artifact of the map-making process. The color scale is in instrument units and the coordinates shown are elevation and cross-elevation. The map has been rotated by the parallactic angle of the observation so that North (positive Dec) is up, the same as in the *Herschel* map in Figure 3.8. 64

3.8 *Herschel* co-added map of East Home (RCW 92B) with a white line drawn between the two compact sources. The colorscale is in MJy/sr and the coordinate grid shown is in equatorial coordinates, with RA horizontal and Dec vertical. 65

3.9 Slices through the BLAST-TNG and *Herschel* maps in Figure 3.7 and 3.8 in both the 350 μm and 500 μm bands. The units of the y-axis are

from the *Herschel* map, while the BLAST-TNG data have been scaled so the peaks match. The BLAST-TNG data have more noise because they are taken from the time-stream of a single detector, while the *Herschel* data slice was taken through the final co-added map of the source.

66

4.1 PolKa LIC (line integral convolution) map. The background color is PolKa Stokes I (Jy/beam, contours every 1 Jy/beam from 1 to 6 Jy/beam), and the LIC pattern shows the magnetic field direction inferred from polarization. Note the approximately 90° flips in field direction at the center right of the map near 9h00m20s R.A. and $-44^\circ 31' 00''$ to $-44^\circ 32' 00''$ Dec. This is often an indication of systematic errors in the polarization data.

69

4.2 PolKa polarized intensity (P) map in Jy/beam, masked to only show 3σ polarization detections, using the statistical uncertainty in P which was provided by the PolKa instrument team. According to this map, we have made 3σ detections of P in many parts of the map, however we know that the edges of the map do not have reliable data because the edges are under-sampled. We also see that the region with 90° polarization flips (as seen in Figure 4.1) has made a significant detection of polarization, according to this figure. This discrepancy convinced us that there were large systematic uncertainties in the PolKa polarization data that were not accounted for in the uncertainties provided by the instrument team.

70

- 4.3 PolKa Q map, only showing pixels with 3σ polarized flux detections. The contours show PolKa Stokes I , and the vectors are inferred magnetic field direction from PolKa. Note that this map shows some inconsistencies with the BLASTPol Q map in Figure 4.4, especially on the right side of the map. Note that this Figure uses an early and incorrect version of the mask. The correct map is the one used in Figure 4.2, which mainly differs by more masked data on the right side of the map, and less masked data near the bottom. 71
- 4.4 BLASTPol Stokes Q map (instrumental units) with contours showing BLASTPol Stokes I and vectors showing BLASTPol inferred field direction. The magenta and blue circles show the ALMA field-of-view and inner 30% of the FOV, respectively. In this map, the sign convention for Q matches the PolKa convention so this map can be directly compared with Figure 4.3. 72
- 4.5 Same as 4.3 but with PolKa U instead of Q . Note that this map is largely consistent with the BLASTPol U map shown in Figure 4.6. Especially note the sign of the values, as the units in these maps are not equivalent. Note that this Figure uses an early and incorrect version of the mask. The correct map is the one used in Figure 4.2, which mainly differs by more masked data on the right side of the map, and less masked data near the bottom. 73
- 4.6 BLASTPol Stokes U map (instrumental units) with contours showing BLASTPol Stokes I and vectors showing BLASTPol inferred field

- direction. The magenta and blue circles show the ALMA field-of-view and inner 30% of the FOV, respectively. 74
- 4.7 Histogram of parallactic angles of the PolKa observations of Vela C South Ridge. The median is 79° , which was used to divide the data into two sets for the jackknife tests. 76
- 4.8 $\text{SNR}(P)$ as defined in 4.7 shown for the center of the PolKa map. The contours are at $\text{SNR}(P) = 1$ (red), 2 (light green), and 3 (purple). 78
- 4.9 The red contour is the boundary of the PolKa mask, plotted over the PolKa Stokes I map (Jy/beam). This is the result of jackknife tests and shows the combination of data cuts as defined in equations 4.8, 4.9, 4.10. The blue dashed circle shows the ALMA field of view. 80
- 5.1 *Herschel* column density map of the Vela C Molecular Cloud. The color scale shows the column density in $\log(N_H/1\text{ cm}^{-2})$. The drapery, or Line Integral Convolution (LIC) pattern shows the direction of the magnetic field inferred from BLASTPol 250 μm polarimetry. South Ridge, which is the target of this work, is the large (about 10 pc across) dense structure centered at approximately $(l, b) = (265.8, 1.1)$. Figure from Soler et al. (2017). 82
- 5.2 South Ridge filamentary structure on multiple scales. The map on the left shows *Herschel* column density (measured in A_V) in the color scale with BLASTPol inferred magnetic field direction shown by the black pseudo-vectors. The dashed blue outline shows the boundary of South

Ridge, as defined in Hill et al. (2011). The right panel shows a moment zero ammonia (NH_3) map ($\text{Jy}/\text{beam km/s}$) from the hyperfine (1,1) transition at 23.7 GHz, measured by the Australian Telescope Compact Array (ATCA). Ammonia emission traces high column density areas of the cloud. BLASTPol inferred field direction is again shown in black, and PolKa magnetic field direction is shown in magenta.

84

5.3 Box-and-whisker plot of the distribution (not uncertainty) of inferred magnetic field direction measurements from BLASTPol, PolKa and ALMA polarimetry. The difference between uncertainty and distribution is especially important to note for the PolKa data, which have a very narrow distribution, but a large uncertainty. The PolKa box and whiskers are shown in gray rather than black because this large uncertainty is based on the estimated systematic errors, as discussed in Chapter 4. For all data sets except “ALMA Peak,” all the vectors passing quality cuts from each instrument were included. For “ALMA Peak,” only the vectors within a contour at the I_{max}/e level were included. The orange lines show the circular mean of the angular data, not the median as is typical with box-and-whisker plots.

88

CHAPTER 1

Introduction**1.1. Magnetic Fields and Star Formation**

One of the biggest questions in modern astronomy is: why is star formation so inefficient, and relatedly, what sets the stellar initial mass function (Krumholz & Federrath, 2019)? This question is critical to our understanding of the universe because almost everything else in the universe depends on how stars are born and live their lives. We know that magnetic fields, turbulence, and stellar feedback all contribute to the answer, but we are still unsure about the exact roles each of these play (McKee & Ostriker, 2007; Li et al., 2014). This work is focused on the role of magnetic fields specifically, and in building instruments to indirectly measure the magnetic field in molecular clouds. Zeeman splitting is the only way to directly measure magnetic field strength in molecular clouds, but it is a very difficult measurement to make, and has only yielded a few dozen detections to date (Crutcher, 2012). Measuring magnetic field direction, however, is significantly simpler, and has been done for thousands of sight lines - including entire clouds at arcminute resolution, and for entire sky at low resolution by the *Planck* satellite, using the High-Frequency Instrument (Lamarre et al., 2010; Planck Collaboration et al., 2014, 2015).

To measure magnetic field directions, we use dust emission polarimetry. Asymmetric dust grains emit polarized light and tend to align themselves perpendicularly to the magnetic field, so polarized dust emission measures the magnetic field direction, projected on the plane of the sky (Hoang & Lazarian, 2008). While this measurement is easier than Zeeman measurements, it still suffers from some difficulties. Primarily the difficulty lies in the wavelength-dependent transmission of the atmosphere. The atmosphere is strongly absorptive and emissive in the submillimeter, which is where the emission spectrum of dust in molecular clouds peaks. Therefore, to observe the dust requires ground-based telescopes at high elevation in dry environments, or telescopes that operate above the atmosphere, either from satellites or from high-altitude balloons.

1.2. BLAST

1.2.1. BLAST Flight History

BLAST, The Balloon-borne Large Aperture Submillimeter Telescope, is one such telescope that operates from a high-altitude balloon. Since 2005, BLAST has had 5 long-duration flights, one from Sweden and four from Antarctica. During the 2006 Antarctic flight, BLAST mapped external galaxies at 250, 350, and 500 μm simultaneously and measured the star formation history of the universe (Devlin et al., 2009; Marsden et al., 2009; Pascale et al., 2009). BLAST was then upgraded to BLASTPol (The Balloon-borne Large Aperture Submillimeter Telescope for Polarimetry), which was capable of measuring the polarization of dust emission. In 2012, BLASTPol made the first high-resolution map of an entire giant molecular cloud. That map of the Vela C molecular cloud remains the

most detailed polarization map of a high-mass star forming region ever made (Fissel et al., 2016; Soler et al., 2017; Fissel et al., 2019).

After the flight in 2012, the BLAST collaboration upgraded the experiment again, calling it BLAST-TNG, or BLAST–The Next Generation. We designed an instrument with a larger, carbon-fiber mirror (Lourie et al., 2018a), a new cryogenic receiver with a longer hold time (Galitzki et al., 2016), and state-of-the-art microwave kinetic inductance detectors or MKIDs (Mauskopf, 2018). The larger mirror and higher number of detectors increased our sensitivity, while the new receiver increased our maximum flight time. MKIDs are frequency multiplexed, so we could read out ten times as many detectors as BLASTPol (3318, Lowe et al. (2020) instead of 270, Galitzki et al. (2014)) with only five readout lines (compared to one line per detector in BLASTPol). We predicted the maximum hold time of the cryostat to be about 24 days, or twice the length of the BLASTPol 2012 flight (Lourie et al., 2018b). We also expected to make eight times as many independent magnetic field measurements, at a higher angular resolution.

We integrated BLAST-TNG in Antarctica in November-December of 2018, and had four launch attempts in December 2018 and January 2019. However, we were not able to launch before the summer anti-cyclone winds began to slow, which ended the launch season. We returned in November 2019, and launched BLAST-TNG on January 6, 2020, the seventh launch attempt of that season. Several seconds after the launch, a piece of equipment from the balloon impacted the payload, damaging a structural component. Despite this, we were able to operate the telescope without issue for nine hours, when we lost pointing control. However, this was enough time to demonstrate that key systems, including our detectors, cryogenics, and pointing, were all functioning as designed.



Figure 1.1. BLAST-TNG on the flightline with the balloon almost entirely inflated. The balloon is visible on the left, with the launch vehicle and BLAST-TNG on the far right. This picture was taken a few minutes before launch.

We terminated the flight after 15 hours because the loss of pointing control meant we would not be able to observe any of our scientific targets. However, this flight was a technology demonstration success, because we operated the first kilo-pixel MKID array from stratosphere, showing that this new technology can be used on future balloon and satellite missions.

1.2.2. BLAST-TNG

Two photographs of BLAST-TNG with the major systems labeled are shown in Figures 1.2 and 1.3. BLAST-TNG is built on a gondola with two separate frames, the “inner” and “outer” frames. The inner frame is mounted onto the outer, and rotates in elevation, while the entire gondola rotates in azimuth for full pointing. All optics and the receiver are located on the inner frame, and therefore move together. A large asymmetrical carbon fiber sun shield is also mounted on the inner frame, which allows us to point as close to the sun as 35° in azimuth. For more information on the pointing system, see Chapter 2.

Much of the design of BLAST-TNG is driven by our detectors. MKIDs offer a huge advantage in terms of multiplexing ability, but they also operate at 270 mK (McKenney et al., 2019). To achieve these sub-Kelvin temperatures, we built a multi-stage cryostat. The first stage was cooled by liquid helium-4, which has a boiling point of 4.2 K at 1 atm. In flight, we used a passive pressure regulator to maintain 1 atm of pressure in the helium-4 tank. Helium from the main bath was also used to fill a “pumped pot,” a small vessel designed to hold liquid helium that is connected to a vacuum pump. By reducing the pressure in the space above the liquid helium, we reduced the boiling point of the helium to 1.2 K. This is low enough to condense helium-3, which is held in a separate, sealed vessel, known as a helium-3 refrigerator. This refrigerator has the same operating principle as the pumped pot, but the pumping action is provided by activated charcoal. When all the helium-3 is adsorbed onto the charcoal, the charcoal can be heated, which releases the helium, and it is re-condensed by the 1.2 K stage.

When cooled to 270 mK, MKIDs operate using a super-conducting resonating circuit. When light strikes the detector, it breaks apart Cooper pairs in the superconducting wire,

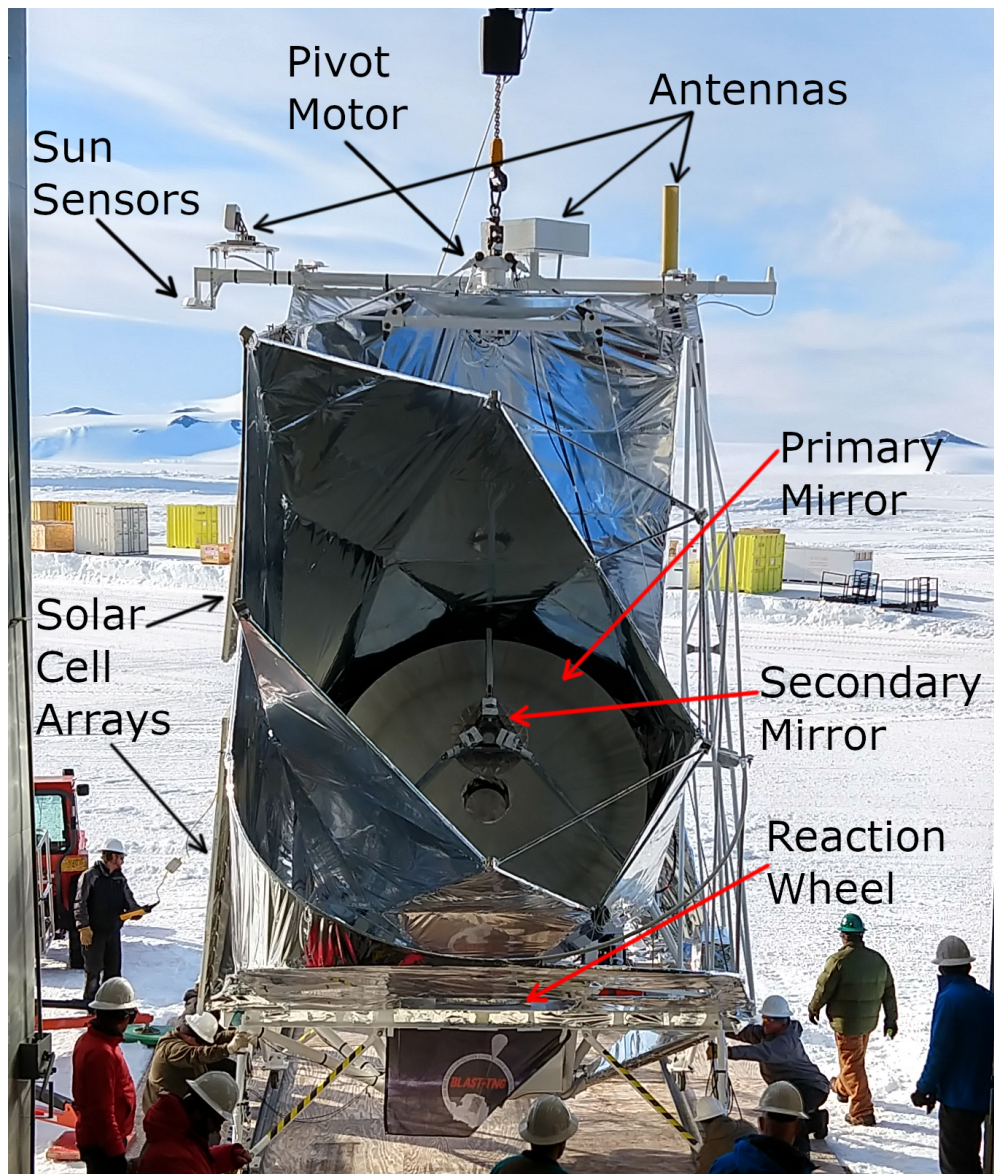


Figure 1.2. Front view of BLAST-TNG with major systems labeled. The primary and secondary mirror are both mounted on the inner frame, which can move in elevation (driven by the elevation motor). The pivot motor and reaction wheel rotate the entire gondola in azimuth. See Figure 1.3 for a side view. Three of the antennas we use to communicate with the payload during flight are visible on the top of the gondola. The solar panel arrays, which power the instrument in flight, are folded close to the gondola in this configuration. Before launch they are unfolded so they face 110° to the right of the front of the telescope.

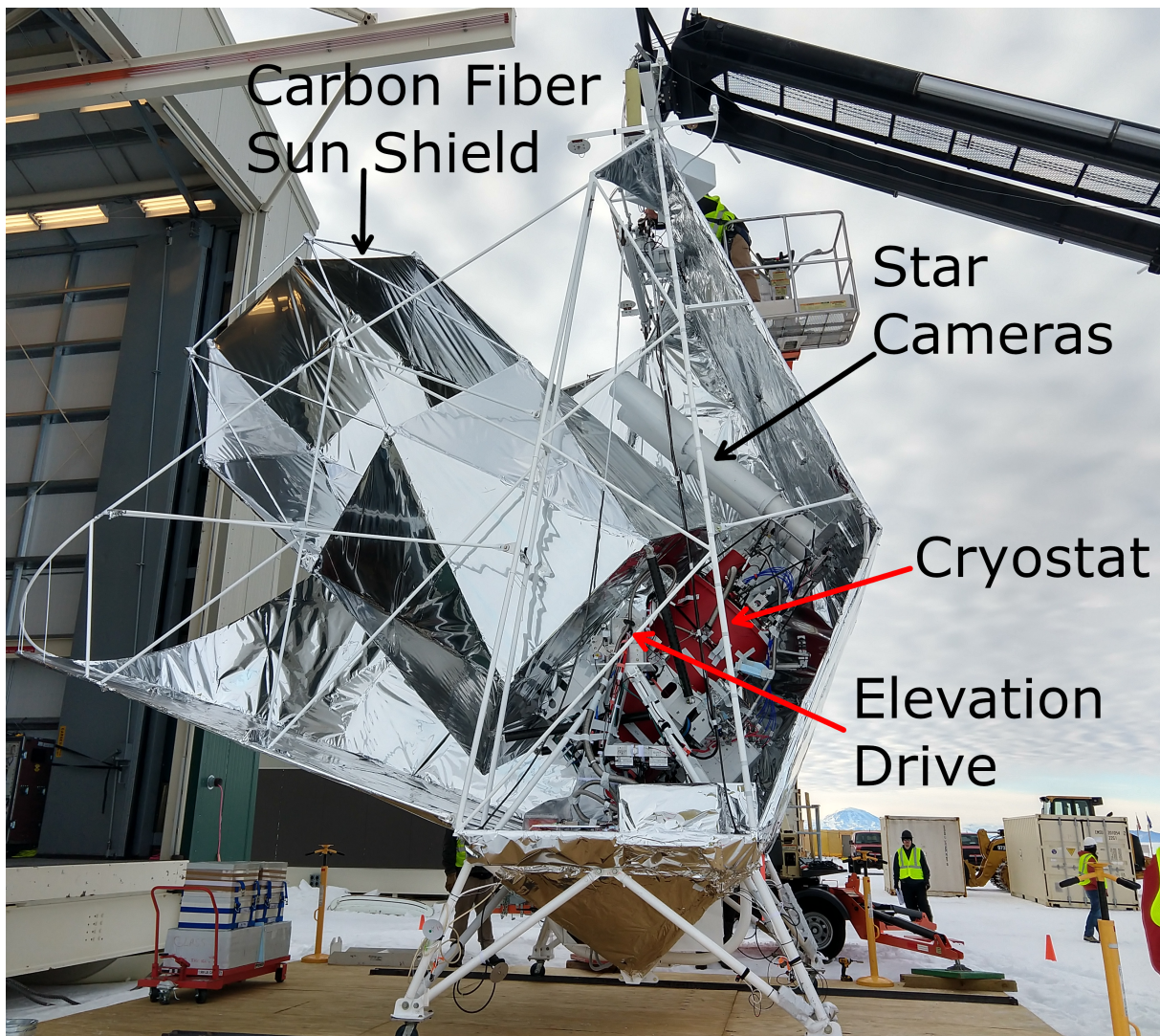


Figure 1.3. Side view (port) of BLAST-TNG with major systems labeled. The star cameras, cryostat, and carbon fiber sun shield, together with the primary and secondary mirrors (shown in Figure 1.2), are all mounted on the inner frame, which moves in elevation (driven by the elevation motor). The sun shield mounted on the back and sides of the gondola is covered in aluminized mylar on the back and starboard side because we keep those sides facing the sun during flight. The highbay is the building with the large open doors on the left. The black structure in the upper right that the instrument is suspended from is part of the launch vehicle.

which changes the kinetic inductance of the circuit. The circuit also contains a capacitor, which makes the circuit a resonator. The resonant frequency of the circuit changes as the kinetic inductance changes. An AC signal with microwave frequency is passed through the array, and each detector absorbs this signal at its resonant frequency. After the signal leaves the array, it is passed out of the cryostat, digitized, and recorded by the FPGA (field-programmable gate array) readout system. By measuring the resonant frequency shift of each detector, we can calculate the amount of light incident on each detector as a function of time. To measure the light polarization, each detector has two resonators, each one sensitive to perpendicular polarizations. To sample both Q and U Stokes parameters (see Section 1.4), we arrange some detectors as shown in Figure 1.4, and others offset by 45° (Dober et al., 2016). For information about the properties of MKIDs, see Mauskopf (2018), Austermann et al. (2018), and Day et al. (2003).

The primary mirror for BLAST-TNG also used a novel technology. A carbon fiber structure minimized the weight, while allowing us to have a larger mirror than previous flights, which increased the angular resolution of the instrument. The primary was 2.5 m in diameter, which determined the size of the overall gondola. The carbon fiber sun shields, for instance, had a larger diameter so they could surround the mirror. In the flight configuration, our gondola nearly filled the size envelope for a balloon payload launched from Antarctica, and was a very tight fit in the highbay¹. This large size and the mylar-covered sun shielding were partially responsible for the difficulty launching the instrument: we required extremely low speed winds, otherwise the wind would cause the instrument to swing dangerously while suspended from the launch vehicle.

¹A highbay is a large hangar-like lab space used to integrate large experiments like BLAST. The highbay in Antarctica is visible on the left side of Figure 1.3

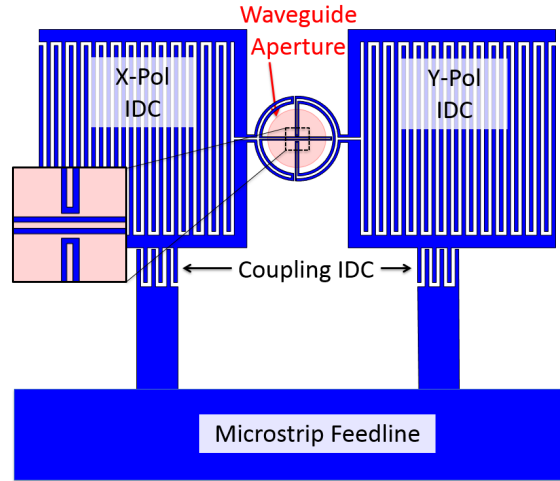


Figure 1.4. Diagram depicting the basic MKID polarimeter design consisting of two detectors, each sensitive to one of two orthogonal linear polarizations. The capacitors are labeled as “IDCs” in this figure, which stands for inter-digitated capacitor, a type of capacitor with inter-laced digits, like those shown in this figure.

1.3. Linking Magnetic Fields Across Spatial Scales

Around the same time that we launched BLAST-TNG, we received data from ALMA observations of a small region in Vela C. ALMA is the Atacama Large Millimeter/sub-millimeter Array (Brown et al., 2004), an interferometer made of 66 individual antennas on the Chajnantor Plateau in Chile. These data are complementary to those from BLAST-Pol’s 2012 flight, meaning we could use the two sets of observations together to map the magnetic field from cloud scales measured by BLASTPol to the resolution of the ALMA data. These ALMA data have a resolution of $2.2''$, or about 2000 AU at the distance of Vela C, which is sufficient to resolve star-forming cores. The maximum recoverable scale of these data is $19''$, which is much smaller than the BLASTPol resolution of $2.5'$. To bridge this gap, we obtained data from PolKa, the Polarimeter für bolometer Kameras

(English: Polarimeter for bolometer cameras) (Wiesemeyer et al., 2014), an instrument on the APEX telescope. APEX, the Atacama Pathfinder Experiment (Güsten et al., 2006), is a 12 m submillimeter telescope also on the Chajnantor Plateau. PolKa is designed to work with multiple bolometer cameras and enables them to make polarimetric measurements. When used with LABOCA (The Large APEX BOLometer CAmera, Siringo et al. (2009)), a 295-pixel 870 micron submillimeter camera used at APEX, PolKa allows polarization measurements that are sensitive to scales from $2.5'$ to $18''$. This range of scales makes it possible to link BLASTPol and ALMA magnetic field measurements, as can be seen in Figure 1.5.

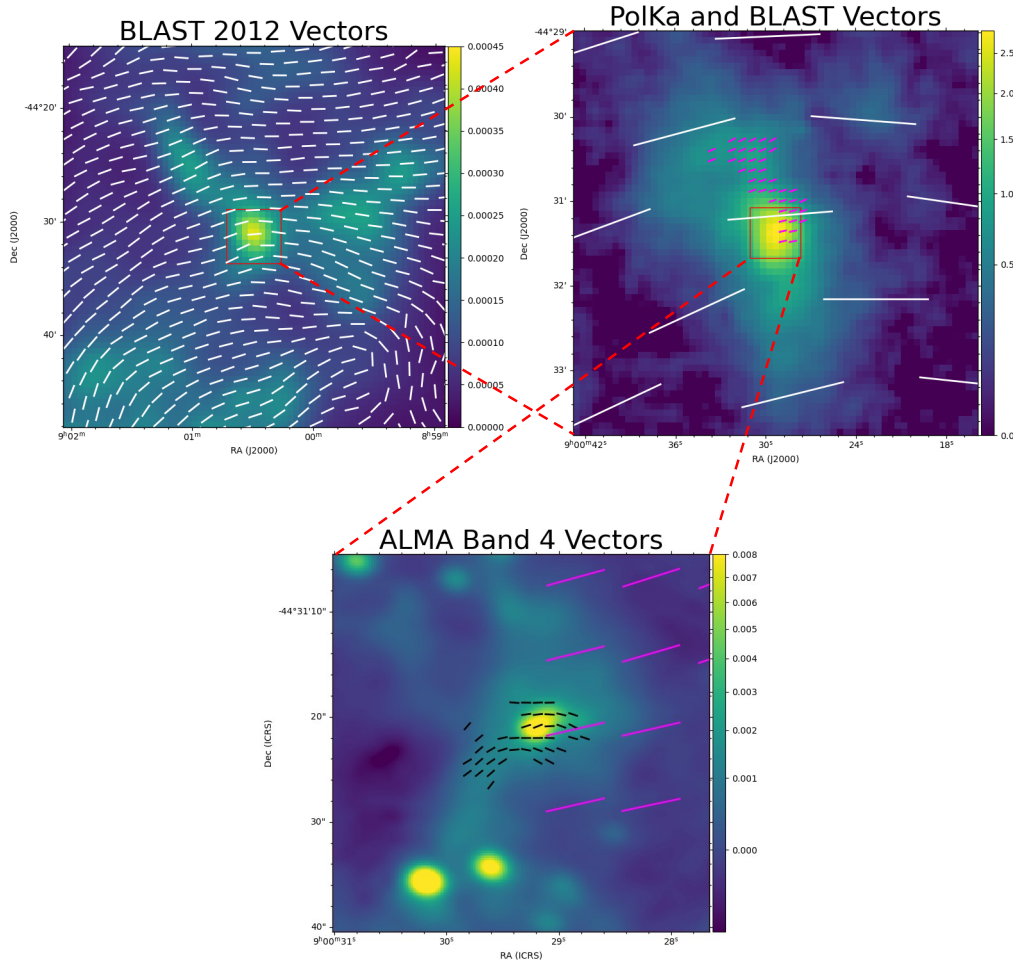


Figure 1.5. This shows the overlap in spatial scales for the BLASTPol, PolKa, and ALMA magnetic field measurements. The top left panel shows BLASTPol 500 μm Stokes I (in instrument units) with BLASTPol inferred magnetic field direction in white vectors. The top right panel shows LABOCA 870 μm Stokes I (Jy/beam) with PolKa inferred field direction in magenta, and BLASTPol in white. The bottom panel shows ALMA 2 mm Stokes I (Jy/beam) with ALMA inferred field in black, and PolKa in magenta. The top right image is about 12 pc across, the top left is 1 pc, and the bottom image is about 0.1 pc across.

1.4. Stokes Parameters and Instrumental Polarization

Some terms specific to polarimetry will be helpful in understanding this dissertation, so we will define them here.

Stokes parameters are the most common way to describe the full polarization of light. The first parameter is Stokes I , or *total intensity*. This is equal to the intensity of the polarized and unpolarized components. The sum of the other three Stokes parameters, Q , U , and V is always equal to or less than I , that is:

$$(1.1) \quad I \geq Q + U + V$$

When the left and right sides of Equation 1.1 are equal, the light is fully polarized. The quadrature sum of the polarized components is often known as the *polarized intensity*:

$$(1.2) \quad P^2 = Q^2 + U^2 + V^2$$

Stokes Q , U , and V are defined experimentally, using the following equations for light traveling along the z axis in a Cartesian coordinate frame.

$$(1.3) \quad Q = E_x^2 - E_y^2$$

$$(1.4) \quad U = E_a^2 - E_b^2$$

$$(1.5) \quad V = E_r^2 - E_l^2$$

In these equations, E indicates the time-averaged electric field, measured parallel to a given basis vector, and the subscripts indicate which basis vector to use. The basis vectors x and y are unit vectors along the x and y axes, and a and b are perpendicular to each other and rotated 45° from the x and y axes. The basis vectors r and l are defined for circularly polarized light, and rotate at the frequency of the light. For the general case of elliptical polarization, all three of Q , U , and V are nonzero. However, for submillimeter dust emission, it is unexpected that $V \neq 0$, so we often rewrite Equation 1.2 as:

$$(1.6) \quad P^2 = Q^2 + U^2$$

For a visual explanation, see Figure 1.6 which shows how these Stokes parameters are defined.

In practice, we can measure Stokes Q with two sets of detectors, one sensitive to vertically polarized light, the other to horizontally polarized light. These detectors can also be used to measure U by using a half-wave plate to rotate the plane of polarized light by 45° , or additional detectors sensitive to light polarized along a and b can be used. Measuring V requires using a quarter-wave plate, or coherent detectors, such as those used in radio astronomy.

Instrumental polarization is a source of error in polarimetry, and occurs when the instrument converts some unpolarized light to Q , U , or V .

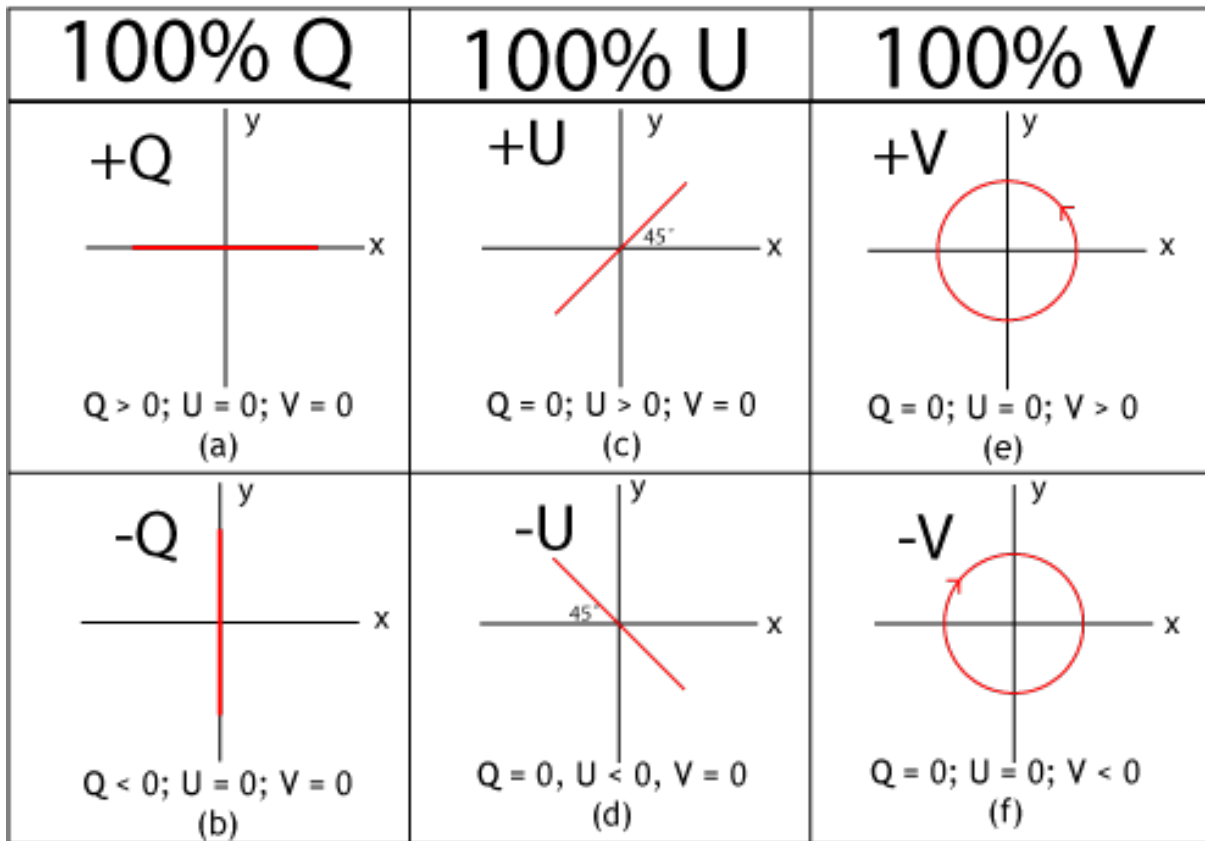


Figure 1.6. Depiction of the polarization of light corresponding to the three polarized Stokes parameters (Q , U , V). In each case, the red line or circle indicates the path traced by the tip of the electric field vector, viewed from the point of view of the source (the convention for circular polarization used in radio astronomy). Image credit: Dan Moulton, used under the terms of CC BY-SA 3.0.

1.5. Outline

This dissertation is organized into six chapters, including this introduction and a conclusion. First we discuss the BLAST-TNG pointing system in Chapters 2 and 3. Initially we describe the BLAST-TNG pointing system, with a focus on one of the components developed at Northwestern, the pinhole sun sensors. Then we discuss one of the key post-flight analyses done at Northwestern, the first order pointing reconstruction using

the coarse pointing sensors. We then discuss linking BLASTPol and ALMA polarimetry, which required significant analysis of PolKa data, which is described in Chapter 4. We then describe our initial conclusions from this linkage in Chapter 5.

CHAPTER 2

BLAST-TNG Pointing System

BLAST-TNG is a scan-mode telescope, and the axes we point in are azimuth (az) and elevation (el). While observing a source, we generally scan quickly ($0.1^\circ s^{-1}$ - $0.2^\circ s^{-1}$) in az while slowly scanning in el. To control the gondola, we use three DC motors, which are described in section 2.1. To determine our attitude during scans, we use multiple pointing sensors, each taking advantage of different strengths, which are described in section 2.2. Pointing control is described in section 2.3.

2.1. Pointing Motors

To control the attitude of the telescope, we have three brushless, direct drive DC motors, the reaction wheel motor (Kollmorgen D063M-22-1320), the pivot (custom, a frameless motor mounted in our pivot), and the elevation drive (Kollmorgen C053A-13-3305). We control the telescope scan speed separately in az and el, using three pointing motors. The elevation motor controls el scan speed, while the pivot and reaction wheel work together to control az scan speed. More information on the pointing control is found in section 2.3.

2.2. Pointing Sensors

Our attitude determination system consists of three types of components, high-accuracy pointing sensors, low-accuracy (“coarse”) pointing sensors, and gyroscopes. The pointing

solutions from the high- and low-accuracy pointing sensors are weighted by their accuracies and combined into pointing solutions at each time. This pointing solution is evolved in time by integrating the velocity data from the gyroscopes (KVH Industries DSP-1760).

Our high-accuracy pointing sensors are two identical, optical star cameras (properties in Table 2.1), and a high resolution elevation encoder. The star cameras are triggered to take exposures at the turnarounds in azimuth, so that the telescope’s angular velocity is lowest and the stars in the images will not be streaked. As a result, the typical interval between star camera images is about 20 seconds, depending on the scan speed and size of the region we are scanning. The star cameras run STARS (Chapman et al., 2014), a “lost in space” algorithm on every image, which does not take into account any prior pointing information to solve for a pointing solution.

Star Camera Properties		
	Pixels	1392×1040
	Pixel Size	$6.45 \mu\text{m} \times 6.45 \mu\text{m}$
Peak Quantum Efficiency		60%
Dynamic Range		14 bit
Well Depth		$16,000 e^-$
Read Noise		$6.5 e^-$
Pixel FOV		7"
Camera FOV		$2.5^\circ \times 2^\circ$
Lens Diameter		100 mm
Len F/#		2
Lens Optical Efficiency		0.8
Filter cut-off		600 nm

Table 2.1. Star Camera Properties: The two star cameras flown on BLAST-TNG were identical and were both mounted parallel to the boresight of the telescope.

During the 2020 flight of BLAST-TNG, the star cameras performed well, but were not always able to solve for a pointing solution due to the presence of polar mesospheric

clouds (PMCs), which reflect sunlight with a strong angular dependence (Thomas & McKay, 1985). PMCs have been observed by previous balloon-borne and ground based experiments, and there is evidence that they reflect thermal radiation from the ground, which can be detected by submillimeter telescopes (Takakura et al., 2019; Miller et al., 2015; Kjellstrand et al., 2020; Geach et al., 2020). As can be seen in Figure 2.1 there was a large variation in light intensity from PMCs in our star camera images, ranging from no obstruction of stars (and no issues solving for a pointing solution) up through complete obstruction. In post-flight analysis, we have been able to use filtering algorithms to successfully recover pointing solutions from many PMC-contaminated star camera images.

Type of Solution	Number of Images Solved
During Flight	593
Total post-flight	1983
Post-flight, no filtering	333
Post-flight, with filtering	1650

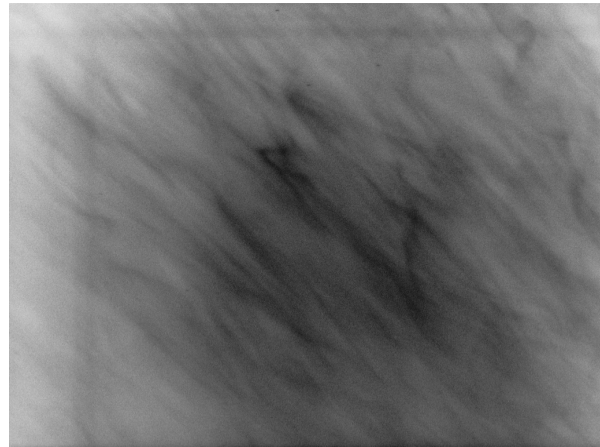
Table 2.2. Star Camera Performance: The total images solved during and after the flight, using STARS (Chapman et al., 2014) during the flight and software from astrometry.net (Lang et al., 2010) post-flight.

This work will continue as we try to recover a high-accuracy pointing solution for the entire length of the flight. The number of star camera images solved during and after the flight are presented in Table 2.2.

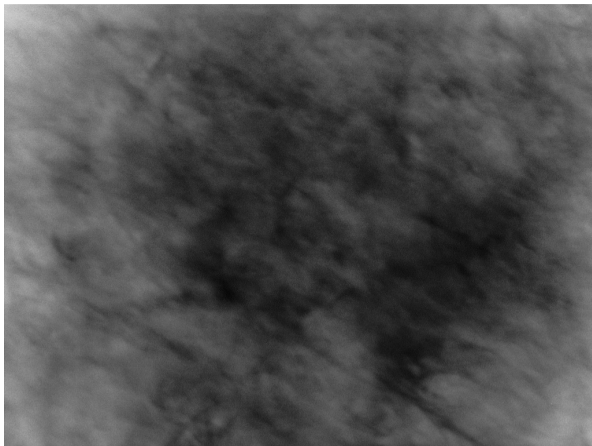
The elevation encoder is read out continuously, and is the only elevation sensor apart from the star cameras. The elevation encoder is especially important for locking the inner frame as it provides a direct measurement of inner frame elevation relative to the outer frame, which is the relevant measurement for locking the inner frame during and prior to both launch and descent.



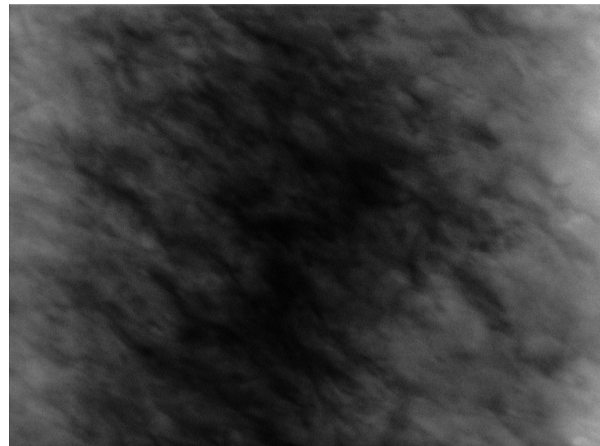
(a) No PMCs



(b) Partial coverage by PMCs, a few stars can be seen, especially near the center-top of the image



(c) Full coverage by PMCs, no stars can be seen



(d) Full coverage by PMCs, even brighter than in 2.1c

Figure 2.1. Example star camera images showing polar mesospheric clouds (PMCs) with various brightnesses. All images have an inverted scale, with bright pixels represented by black and dark pixels represented by white.

The low-accuracy or “coarse” pointing sensors serve two purposes. The first is to give rough pointing solutions if the star cameras are not able to get solutions due to a lack of visible stars, or if planets (which are not in the catalog the star cameras use) are in the fields of view. We also use the coarse pointing sensors to correct for low-frequency noise

Sensor	Location	Rate (Hz)	Accuracy ($^{\circ}$)
Star Cameras	Inner Frame	0.05-0.1	<0.001
Elevation Encoder	Outer Frame	100	<0.01
Pinhole Sun Sensors	Outer Frame	5	0.2
Magnetometers	Outer Frame	100	5
DGPS	Outer Frame	5	0.2
Inclinometers	Both Frames	5	0.1

Table 2.3. Pointing Sensor Properties

in the gyroscope signal. This manifests as a slowly varying DC offset between the true and measured velocities. We use each coarse pointing sensor to calculate our velocity and find the difference between that and the velocity reported by the gyroscopes to correct the gyroscope DC offset. Our coarse pointing sensors include pinhole sun sensors, differential GPS, magnetometers, and inclinometers, and they are summarized in Table 2.3.

The pinhole sun sensors (PSSs) use Hamamatsu S5991-01 position sensitive diodes (PSDs). When the spot of light from the 200 μm pinhole light strikes the PSD, charge proportional to the intensity of the light is generated. We voltage bias the PSD, which causes the generated charge to flow as current to the four electrodes at the corners of the active area, and the relative magnitudes of these currents can be used to determine the spot location using equations 2.1 and 2.2. In these equations, L is the length of the active area of the PSD, and $I_1, I_2, I_3,$ and I_4 are the four measured currents. The pinhole sun sensors provided pointing solutions with precision of 0.18° in the 2010 flight of BLASTPol (Korotkov et al., 2013) and initial results from the 2020 flight of BLAST-TNG show a pointing precision of 0.2° . Calibration of the sun sensors is discussed more in Section 3.2.

$$(2.1) \quad x = \frac{L(I_2 + I_3) - (I_1 + I_4)}{2(I_1 + I_2 + I_3 + I_4)}$$

$$(2.2) \quad y = \frac{L(I_2 + I_4) - (I_1 + I_3)}{2(I_1 + I_2 + I_3 + I_4)}$$

CSBF provides heading information from their differential GPS sensor (DGPS), which we use as an azimuth sensor, and has a precision of about 0.2° when compared with the in-flight star camera solutions. Post-flight calibration of the DGPS is discussed in Section 3.1.

We have two magnetometers (Honeywell HMR2300) on the payload, which we mounted on the sun shields, as far from motors and other active components as possible to minimize the effect of magnetic fields generated by currents in the motors. The magnetometers also provide azimuth information. We compare the magnetic field direction measured by the magnetometers with a model of Earth's magnetic field to get heading information from the magnetometers. This measurement is difficult from Antarctica because Earth's magnetic field is more vertical near the geomagnetic pole, so the horizontal component, which is what we measure to get an azimuth solution, is weaker than in other places on Earth.

We also flew two bubble inclinometers (Applied Geomechanics 904-T), that were mainly useful to reconstruct the event that caused the end of our flight. They confirmed that the outer frame of the gondola was pitched forward by 4° , which was consistent with comparisons between the star camera elevation solutions and the elevation encoder.

2.3. Pointing Control

Our pointing control software uses a proportional-integral-derivative (PID) control loop. For all our scans, we set a desired scan speed, or *set-point*. The PID loop first calculates the error between the measured scan speed and the set-point. This error is represented by $e(t)$, and is a function of time. In general, to find the motor current that we command at the next time step, we calculate Equation 2.3, where $i(t)$ is the motor current. K_p , K_i and K_d are coefficients that adjust the relative strengths of the proportional, integral, and derivative terms, respectively.

$$(2.3) \quad i(t) = K_p e(t) + K_i \int_0^t e(t') dt' + K_d \frac{d}{dt} e(t)$$

These coefficients can be changed during the flight by sending commands to the payload. In our tests, we found that the derivative term did not significantly improve our pointing performance, so we set $K_d = 0$ for the flight, and the rest of this section will discuss only the P and I terms.

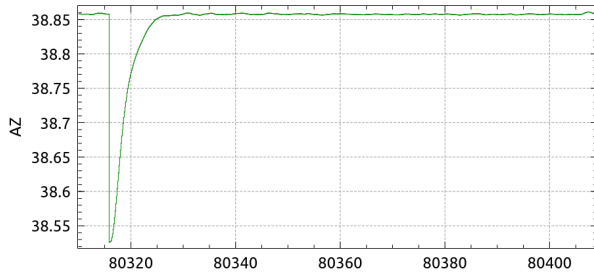
The elevation control loop is relatively simple. We choose a elevation scan speed set-point, and calculate the modified Equation 2.3, which is shown in Equation 2.4. The calculated current, i_{EL} is then commanded to the elevation motor at the next time step.

$$(2.4) \quad i_{EL}(t) = K_{p,EL} e_{EL}(t) + K_{i,EL} \int_0^t e_{EL}(t') dt'$$

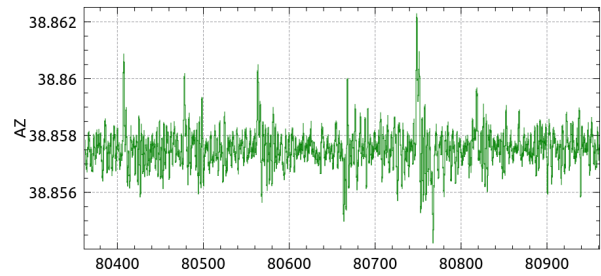
The az control loop uses the pivot and reaction wheel each to perform slightly different tasks. The reaction wheel is a large (~ 1 m diameter) wheel with a large moment of inertia (~ 50 kg m). It is driven by a brushless DC motor that can transfer angular momentum between the reaction wheel and the rest of the payload very quickly, so by setting high PI coefficients, the reaction wheel exerts most of the torque needed for our maneuvers. However, the reaction wheel has a maximum speed of about 300° s^{-1} or 50 rpm, when motor saturates due to back EMF. The pivot motor cannot exert as much torque as the reaction wheel motor because it torques against the balloon through the flight train, which can be modeled as a torsion spring with a very low spring constant. We therefore use the pivot to slowly shed excess angular momentum and keep the reaction wheel rotating at a speed much less than the saturation point, typically at 30° s^{-1} . The pivot is also used to point directly, so it has two sets of PI terms, one set that uses the error in the reaction wheel velocity, and the other that uses the error in the azimuth scanning speed. Equations 2.5 and 2.6 show how we calculate the currents for the reaction wheel and pivot. Each term calculated from the az scan speed error, e_{AZ} , has a coefficient K_X and these are adjusted such that the reaction wheel is responsible for most of the azimuth control. The pivot Equation (2.6) has a second set of PI terms that respond to the error in the reaction wheel velocity, $e_{RW}(t)$. In all cases, the integral coefficients K_i are inversely proportional to the time period over which the integral terms become important, and are again set so that the reaction wheel is responsible for most of the fine azimuth control, while the pivot primarily operates to shed excess angular momentum and to keep the reaction wheel from saturating.

$$(2.5) \quad i_{RW}(t) = K_{p,RW}e_{AZ}(t) + K_{i,RW} \int_0^t e_{AZ}(t') dt'$$

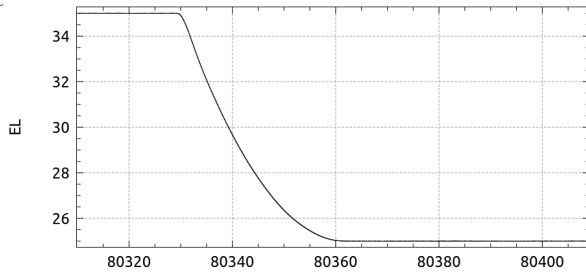
$$(2.6) \quad i_{PIV}(t) = K_{p,PIV}e_{AZ}(t) + K_{i,PIV} \int_0^t e_{AZ}(t') dt' \\ + K_{p,PIV-RW}e_{RW}(t) + K_{i,PIV-RW} \int_0^t e_{RW}(t') dt'$$



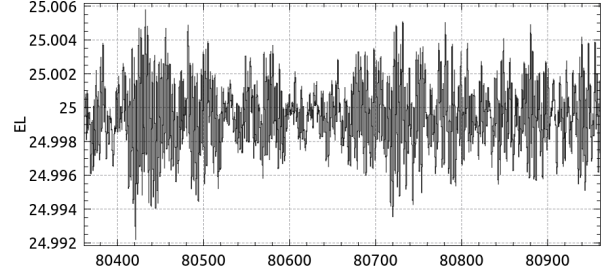
(a) Az coordinate during az-el go to



(b) Az coordinate after az-el go to



(c) El coordinate during az-el go to



(d) El coordinate after az-el go to

Figure 2.2. Example of an az-el go to command showing the pointing stability of BLAST-TNG. In this example, stability is $2.4''$ in az and $7.1''$ in el. This is calculated from the standard deviation in az and el over ten minutes, during the period shown in Figures 2.2b and 2.2d. The horizontal axes in all 4 plots are in seconds, and the vertical axes are in degrees.

During flight, we use multiple pointing modes, all of which are based on velocity control using the PID control loop described above. The simplest mode is “drift,” which uses feedback from the gyroscopes to move the telescope at a constant speed in both azimuth and elevation. A special case of “drift” is “stop” where both speeds are set to zero. We have two “go to” modes, one which goes to a position in az and el, while the other tracks a position in right ascension and declination. For scanning science and calibration targets, we use “box” mode most often which scans a rectangle with a center in ra and dec, and the box size defined in az/el.

For an example of the results of an in-flight az/el go to command and the pointing stability of the system, see Figure 2.2. We find that over ten minutes, our pointing is stable to 2.4'' in azimuth and 7.1'' in elevation.

2.4. Pinhole Sun Sensor Design and Construction

As described in Section 2.2, the pinhole sun sensors are an array of pinhole cameras that observe the position of the sun in order to reconstruct coarse azimuth pointing. We designed the array of eight PSSs on BLAST-TNG so that they had overlapping fields of view and at least one could view the sun through 180° of azimuth. Due to our gondola design, we can only point through about 140° of azimuth, relative to the sun. Our asymmetric sun shields allow us to point from -180° to -40° azimuth, measured relative to the sun.

We built the pinhole sun sensors (PSSs) primarily from off-the-shelf components using our own design that was based on the sun sensors that flew on BLASTPol in 2010 and 2012. The main differences for BLAST-TNG were: (1) we had eight PSSs rather than the

two or four which were flown in 2010 and 2012, and (2) we mounted the PSSs relatively far from the flight computers, which meant using an ethernet-enabled analog-to-digital converter (ADC) to read out the PSSs.

We required an ADC that could digitize 40 channels (see below) at a rate of at least 5 Hz, and stream them to our flight computers in real time. We chose the Labjack T7—its specifications, and those of an alternative ADC we also considered, are summarized in Table 2.4. Given that storage temperature ranges often exceed operating temperature ranges, and that the operating range of the T7 is identical to the storage temperature range of the National Instruments sbRIO, we were not concerned that a storage temperature was not specified for the Labjack T7.

It has several communication modes, but in the fastest mode, it can stream up to 100,000 samples/second (where samples/second is the number of channels times the rate of each channel). This means we could easily stream the 40 channels we had for the PSSs (5 channels per PSS, 4 for the sun position information and 1 temperature channel) at 10 Hz. In fact, the T7 performed so well in initial tests for the PSS that we decided to use it to read out and control several other telescope systems, including: cryostat and gondola thermometry readout, cryostat heater control, magnetometer readout, and gas flow meter readout. We also found that the regular (non-OEM) T7 was better suited to our needs because the provided enclosure was easy to remove and the regular version came with all the connectors we needed soldered to the board.

Table 2.4 mentions the Mux80, which is a multiplexer accessory compatible with the T7. The T7 has 14 analog input channels, the Mux80 takes 10 of these and multiplexes them by a factor of 8, giving 84 total channels in single-ended mode, or 42 channels in

ADC	Labjack T7- OEM w/Mux80	National Instruments sbRIO
Price	\$478	\$4781
Operating Temperature (°C)	-40 to 85	-20 to 55
Storage Temperature (°C)	N/A	-40 to 85
Power (W)	1.4	7.5
Resolution (bits)	16	16
Range (V)	(-10) - 10	(-10) - 10
Channels	84 (w/MUX)	32
Non-volatile memory	Flash	Flash & EEPROM
Memory amount (MB)	4	128
Availability	In Stock	12-20 days
Size (in)	8 x 4	8.2 x 5.6
Notes	price includes \$149 for Mux80	price includes \$2999 for LabVIEW

Table 2.4. Specifications for the final two ADCs we considered for the Pin-hole Sun Sensors. The two blank cells for the Storage Temperature and Weight of the Labjack T7 are specifications that we were unable to find prior to deciding which to buy. The quotes given are from late 2015.

differential mode. We used the same ground for the T7 and the sun sensors, so we used the T7's ADC functionality in single-ended mode.

We also built an enclosure for the T7, the Mux80, a DC/DC power converter to power the T7 from the 24 V gondola power supply, and terminal blocks to route power to the PSSs and returning signals. A photograph of this enclosure in the early stages of development is shown in Figure 2.3.

We designed the pinhole sun sensors and machined the parts out of aluminum. It was necessary for the PSSs to be able to view the sun at any time of day on the summer

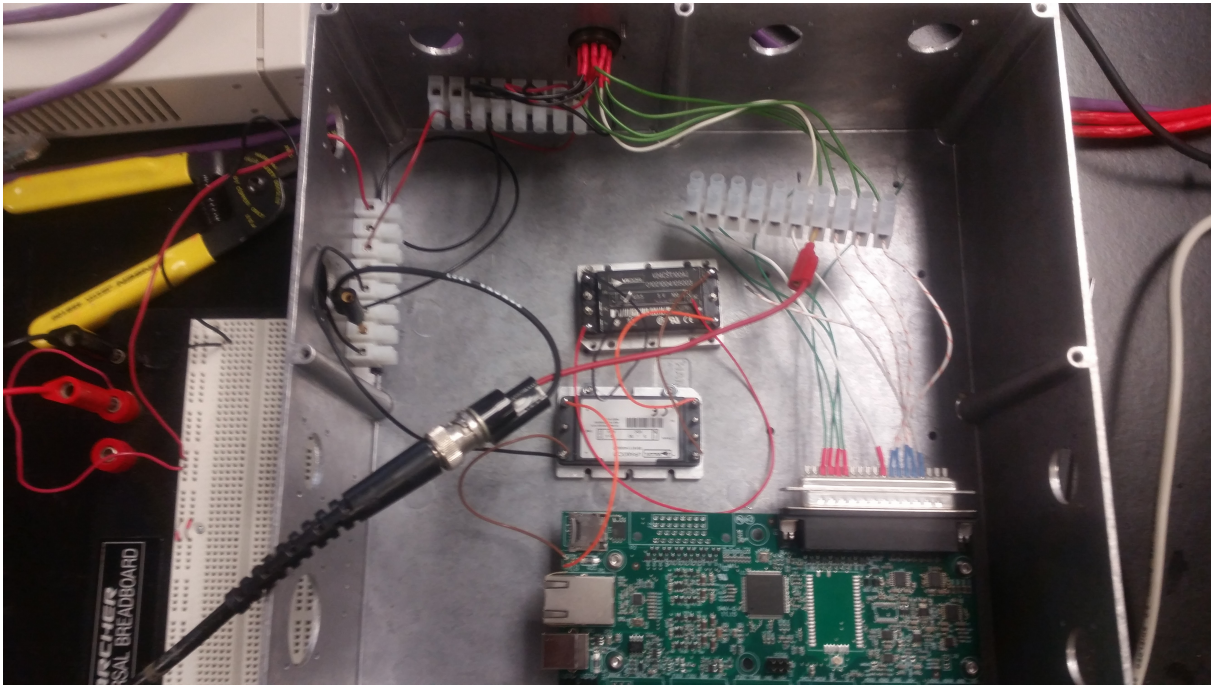


Figure 2.3. The enclosure for the PSS Labjack T7 in an early stage of development. The T7 is the large printed circuit board in the lower right of the image. The small black and silver electrical components in the center are the DC/DC converter and micro ripple attenuator modules, which we use to convert and condition the 24 V battery power available on the gondola to 5 V for use by the T7. This version of the T7 box did not use the Mux80 multiplexer board, which plugs into the T7 at the DB37 connector on the upper right of the PCB. In the flight version, the T7 was connected to the gondola network via ethernet.

solstice from 10° latitude north of the launch site at McMurdo Station, Antarctica. In our design, the FOV of each PSS was 40° and the elevation mounting angle was 25° . Therefore, we could observe the sun at any elevation from $5^\circ - 45^\circ$. The FOV was also 40° wide, which meant that eight sun sensors could cover 180° of azimuth, with overlap for redundancy. Due to unidentified hardware problems, only six of the eight the sun

sensors were functional enough to be integrated for the flight. The overlapping fields-of-view allowed us to mount these six such that they covered about 165° of azimuth, which was sufficient to observe the sun during almost the entire flight.

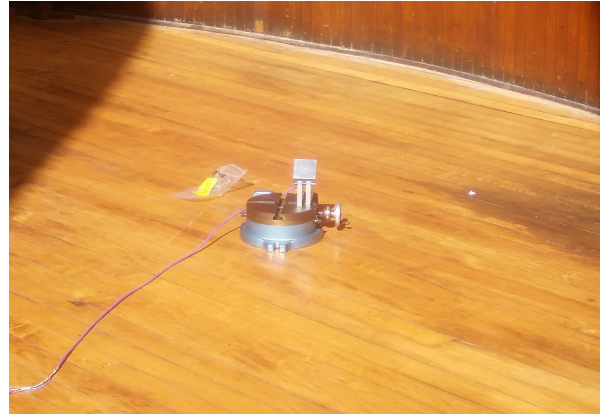
The electronic components of each PSS were surface-mounted on custom printed circuit boards. The populated circuit boards were installed in the machined cameras, with commercial precision $200\mu\text{m}$ pinholes mounted in front of the position sensitive diodes. To test basic functionality, we connected one PSS to the T7 and checked that the voltages varied as we moved a light source in the field-of-view.

We also tested the performance of one sun sensor when it was observing the sun. This required a location with both electrical power (to power the T7 and sun sensor) and a view of the sun. To find both of these, we used the Dearborn Observatory on Northwestern's Evanston campus. During the day, with the dome open, we could observe the sun and power our devices. Photos of our calibration setup are shown in Figure 2.4.

When BLAST-TNG was assembled prior to launch, we did some pointing testing and calibration. This involved moving the entire instrument to a wooden deck constructed in the snow far from any buildings, and rotating the instrument about the vertical axis several times. Being far from any buildings or other metal structures helped us to calibrate our magnetometers. These tests also helped us get an initial calibration for the sun sensor array. This calibration was incomplete primarily because the sky brightness on the ground causes the values of x and y in Equations 2.1 and 2.2 to decrease, which changes the calibration parameters. Therefore the final calibration is only possible during the flight.



(a) The readout portion of the PSS testing and calibration setup. This picture shows the Lab-jack T7 box, power supplies, and a laptop to display signals read by the T7. The red cable on the right is connected to the purple one in Figure 2.4b.



(b) One PSS mounted on a rotary stage in the center of the photo in the sun. The purple cable connected the PSS going to the left is connected to the red cable on the right of Figure 2.4a

Figure 2.4. PSS testing and calibration setup in Dearborn Observatory.

CHAPTER 3

BLAST-TNG 2020 Flight Pointing Data Analysis

After the flight of BLAST-TNG, we began working on a post-flight pointing solution. We expected that we would be able to calibrate our pointing sensors post-flight in order to get a more accurate and complete pointing solution than the in-flight pointing solution. The flight was so short that we were not able to fully calibrate some sensors during the flight. Also, as mentioned in Section 2.2, our star cameras were not able to obtain solutions throughout much of the flight due to polar mesospheric clouds (PMCs) in the fields of view of the cameras. By calibrating the coarse sensors, we hoped to reconstruct a more accurate pointing solution during the times that the star cameras were blocked by PMCs. We first calibrated the Differential GPS (DGPS), discussed in Section 3.1, and then calibrated the pinhole sun sensors (PSSs), discussed in Section 3.2.

3.1. Differential GPS Calibration

We calibrated the DGPS by comparing its azimuth pointing solution to all the available star camera pointing solutions from the flight. To make this comparison, we first had to synchronize the star camera pointing solutions. The star camera pointing solutions are asynchronous from the rest of the pointing sensors because each camera has its own computer which attempts to solve every image. If it gets a solution, it sends that to the flight computers, but solving the image can take several seconds, so the time the flight computer gets that solution and records it is up to several seconds after the image was

taken. To get the most accurate calibration required synchronizing the solution data with the times that images were taken. The flight computer “triggers” the star camera to capture images at appropriate times, so these triggers are recorded by the flight computer at the time the image was captured. By changing the time on all the star camera solutions from the time the solution was received to the time the trigger was sent, we were able to synchronize the star camera solutions to the rest of the pointing data.

The next step was to compare every star camera solution to the DPGS az solution for the same time. A histogram of $AZ_{XSC0} - AZ_{DPGS}$ is shown in Figure 3.1. The mean of this distribution is 269.6° and the standard deviation is 0.12° . The mean of the distribution can then be used as a calibration parameter to find the equivalent star camera azimuth solution at any time that DPGS had a pointing solution. The large value of the calibration constant is expected, because CSBF uses an azimuth zero point that differs from ours by close to 270° , so this new offset only differs by 0.4° .

This calibration offset can be applied to the DPGS data using Equation 3.1, where AZ_{EST} is the estimate of the true azimuth.

$$(3.1) \quad AZ_{EST} = AZ_{DPGS} + 269.6$$

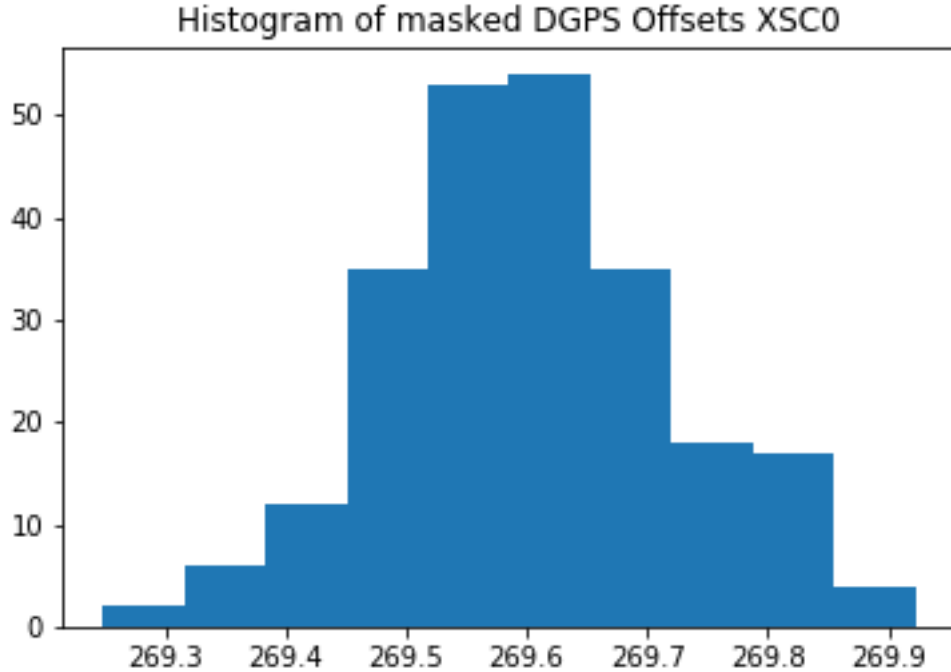


Figure 3.1. Histogram showing the difference between the DGPS and Star Camera 0 (XSC0) azimuth pointing solutions, in degrees. This is based on 236 solutions from XSC0.

3.2. Pinhole Sun Sensor Calibration

After the flight, the first step to calibrating the PSSs was to find an uncalibrated PSS pointing solution from the raw voltage data. This was necessary because we were changing the calibration parameters during the flight, so the in-flight pointing solution from the PSSs did not have a consistent calibration. We did this by re-creating the PSS pointing solution code from flight, but applying it to the entire flight at once.

Our initial calibration of the PSS data from the 2020 flight was to build a model of all the sources of error that would cause each PSS to have a different pointing solution from the star camera pointing solution. The sources of error identified were: (1) an

offset in azimuth between the center of the PSS FoV and the telescope boresight that is different from the nominal one; (2) a roll (or clocking) error in the positioning of the PSD; (3) an offset in cross-elevation of the pointing of the star cameras relative to the telescope boresight; and (4) an error in the gain, or the conversion between the output currents in equations 2.1 and 2.2 and angle on the sky.

These sources of error should explain any difference between the star camera and PSS pointing solutions, so Equation 3.2 was used to fit for the parameters which quantify the sources of error. The parameters we fit for were: G_i , the gain of PSS i ; $AZ_{0,i}$, the offset in az between PSS i and the telescope boresight; C_i , the clocking of each PSD; and $xEL_{SC,j}$, the cross-elevation offset of star camera j with respect to the boresight. $AZ_{wrt\odot}$ is the azimuth of the gondola relative to the sun (instead of north), EL_{\odot} is the sun elevation, and $AZ_{PSS,i}$, $AZ_{SC,j}$, $EL_{SC,j}$ are the az and el measured by PSS i and star camera j . This equation only accounts for the first order effects of these sources of error.

$$(3.2) \quad AZ_{SC,j} - AZ_{PSS,i} = G_i(-AZ_{wrt\odot} - AZ_{0,i}) + C_i(EL_{\odot} - 25^\circ) + \frac{xEL_{SC,j}}{\cos(EL_{SC,j})}$$

To prepare the PSS data for calibrating with this equation, we first implemented some cuts to ensure we were only fitting high quality data. We tested different data cuts, and the final version can be summarized by equations 3.3 to 3.5.

The first cut is on the magnitude of the total voltage measured by a PSS. When the sun is not in the field-of-view of any one PSS, the voltages are all relatively small ($|V| < 0.5$ V). When the sun is in the field-of-view of a PSS, the voltages are significantly higher, generally each of the 4 voltages is around 2.5 V or higher. To easily distinguish

between times a PSS is viewing the sun and times it is not, we required that the sum of the magnitudes of the voltages be greater than 9 V. Note that the four voltages measured are all directly proportional to the currents discussed in Section 2.2 and in Equations 2.1 and 2.2. Equation 3.3 summarizes this data cut, where V_i for $i = 1, 2, 3, 4$ are the four voltages for a single PSS. This data cut is then applied to all 6 PSSs.

$$(3.3) \quad \sum_{i=1}^4 |V_i| > 9 \text{ V}$$

The second data cut, summarized in Equation 3.4, was to make sure that it was reasonable to expect the sun in the field-of-view of a given PSS. We checked this by ensuring that the azimuth of the gondola relative to the sun was within $\pm 20^\circ$ of the center of each PSS, because the full-width field-of-view of each PSS is 40° , as discussed in Section 2.4.

$$(3.4) \quad AZ_{0,i} - 20^\circ < -AZ_{wrt\odot} < AZ_{0,i} + 20^\circ$$

The third data cut, summarized in Equation 3.5, was to ensure that the image of the sun on the PSD was not near the edge of the sensor. The sensor deviates from a linear response near the edge, so we made sure the sun fell within a square 8 mm on a side centered in the middle of the PSD. This excluded a 1 mm boundary around the edge of the PSD.

$$(3.5) \quad \begin{aligned} |X| &< 4 \text{ mm} \\ |Y| &< 4 \text{ mm} \end{aligned}$$

In the course of analyzing the PSS data, we also found issues with two of the PSSs. The first is that during the ascent phase of the flight, the voltages from PSS1 stopped changing and were approximately constant for the rest of the flight. This includes during times that we expected the sun to be in the field-of-view of PSS1. The second issue was that the solutions calculated from PSS5, both during and post-flight, were very different from the values measured by the star cameras or other PSSs. From this we assume that there were hardware problems with PSS1 and PSS5 that we had not discovered before launch. We did not include PSS1 and PSS5 in our post-flight pointing solution.

To calibrate the remaining four PSSs, we first applied Equation 3.2 to each combination of PSS and star camera individually. This gave results that seemed reasonable for the calibration parameters, but they were not always consistent. For example, the calibrations for PSS2 and PSS3, both compared with star camera 1, had different values for $xEL_{SC,j}$, the star camera cross-elevation offset from the telescope boresight. However, this offset is a physical quantity, so there can only be one value for it. To remove this type of error from our calibration, we decided to calibrate all four PSSs and both star cameras simultaneously. We accomplished this using a modified version of Equation 3.2, shown in Equation 3.6. The only difference between these two equations is the presence of delta functions in 3.6. These delta functions ensure that only data from a given PSS

contribute to the value of the calibration constant for that PSS, and the same for both star cameras.

(3.6)

$$AZ_{SC,j} - AZ_{PSS,i} = \sum_{i=2,3,4,6} G_i(-AZ_{wrt\odot} - AZ_{0,i})\delta(i - P) + C_i(EL_{\odot} - 25^{\circ})\delta(i - P) + \sum_{j=0,1} \frac{xEL_{SC,j}}{\cos(EL_{SC,j})}\delta(j - S)$$

The key to these delta functions working are the variables P and S . These are additional variables we created, which are the number of the PSS and the star camera, respectively, that the data are from. This ensures that data from each PSS and star camera only affect the calibration parameters of that PSS or star camera, but that we calibrate all PSSs simultaneously. This simultaneous calibration results in the calibration parameters shown in Table 3.1. A histogram of the residuals of this global fit is shown in Figure 3.2. The standard deviation of the residuals is 0.19° (this is also known as the RMS error). Therefore, this analysis finds that the PSSs were accurate to 0.19° , which is very close to the 0.18° measured in the 2010 flight of BLASTPol. However, as discussed below, we find the accuracy is lower with another method.

To apply this calibration to the sun sensors, we calculated the predicted azimuth offset (the left side of Equation 3.6) using the parameters in Table 3.1, with one small change. We did not have star camera solutions for all the available PSS solutions, so we used the elevation measurement from the elevation motor encoder to get a different set of calibration constants, which we then applied to the entire set of PSS solutions. The

Sensor	Parameter	Value	Uncertainty
PSS2	Gain	0.37	0.009
	AZ ₀	148.3	1.041
	Clock	-0.24	0.034
PSS3	Gain	0.29	0.003
	AZ ₀	99.67	0.97
	Clock	-0.002	0.008
PSS4	Gain	0.30	0.003
	AZ ₀	81.05	0.84
	Clock	-0.16	0.014
PSS6	Gain	0.33	0.012
	AZ ₀	37.80	0.641
	Clock	-0.28	0.015
XSC0	xEL	-2.23	0.187
XSC1	xEL	-1.30	0.186

Table 3.1. The 14 calibration parameters for the simultaneous fit of all 4 PSSs and both star cameras (XSC = star camera). Equation 3.6 was used for this fit.

full solution of all 4 pinhole sun sensors is shown in Figure 3.3, and a part of one scan is shown in Figure 3.4.

One check we performed on the sun sensor calibration was to find the difference between the pointing solutions obtained by PSS3 and PSS4, when the sun was in both of their fields-of-view. This difference, plotted vs time, is shown in Figure 3.5. If the differences between PSS3 and PSS4 were the result of statistical errors, we would expect the distribution of differences to be consistent with the distribution of the fit residuals, which are shown in Figure 3.2. This is not the case, and the differences here have a larger magnitude than the residuals from the fit. This is evidence that some systematic error is playing a role in the accuracy of the sun sensors. The RMS of the difference between PSS3 and PSS4 is 1.4° . Assuming that each sun sensor contributes equally to this RMS, the accuracy of a single PSS is lower by a factor of $\sqrt{2}$, or 1° .

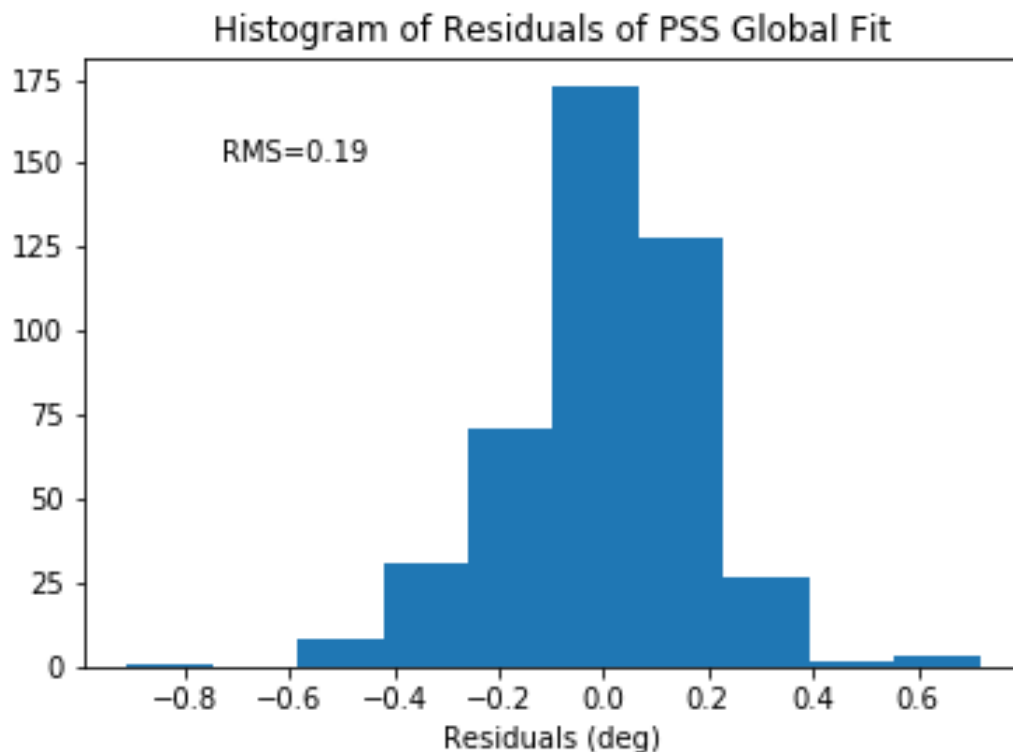


Figure 3.2. Histogram of the residuals of PSS global fit. The 14 parameter fit predicts the difference between PSS and star camera az solutions with an RMS error of 0.19° .

This is a larger uncertainty by a factor of 5, but we were not able to determine why the uncertainty would be so much larger than indicated by the fit. Both of our methods for determining the accuracy have their downsides. In the first case, it is possible that the linear assumptions made in our fitting model break down at the edge of each sensor's field-of-view, which is the only part of the FOV where we were able to make this comparison. In the second case, it is possible that the PSS system did not perform as well as expected, perhaps due to thermal instabilities in the electronics, or thermal deformations in the PSS mounting system.

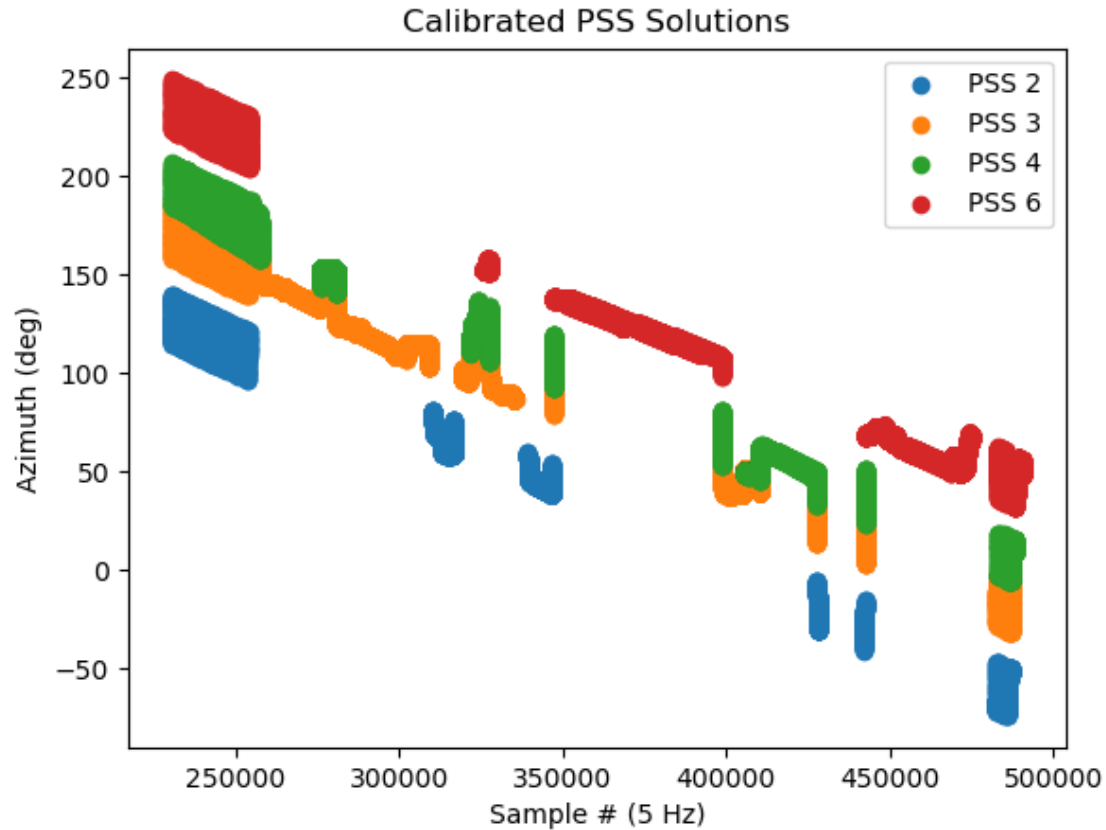


Figure 3.3. The calibrated PSS solutions for the entire flight of BLAST-TNG. Each PSS is shown in its own color, individual solutions are dots, but they mostly blend together at this scale. Each PSS covers a different range of azimuth, which is fixed relative to the sun, but decreases in time (because the sun's azimuth decreases during the day due to the rotation of the Earth). The only two sun sensors which have overlapping fields-of-view are PSS3 and PSS4, which can be seen from this plot by the fact that the green and orange points overlap in several time ranges. At the beginning of the range shown the balloon and telescope were ascending and the telescope was rotating freely through 360° of azimuth, which is why all 4 sun sensors viewed the sun during that time. Expanding the time axis shows that each PSS viewed the sun at separate times, with the exception of PSS3 and PSS4 on the edges of their fields-of-view.

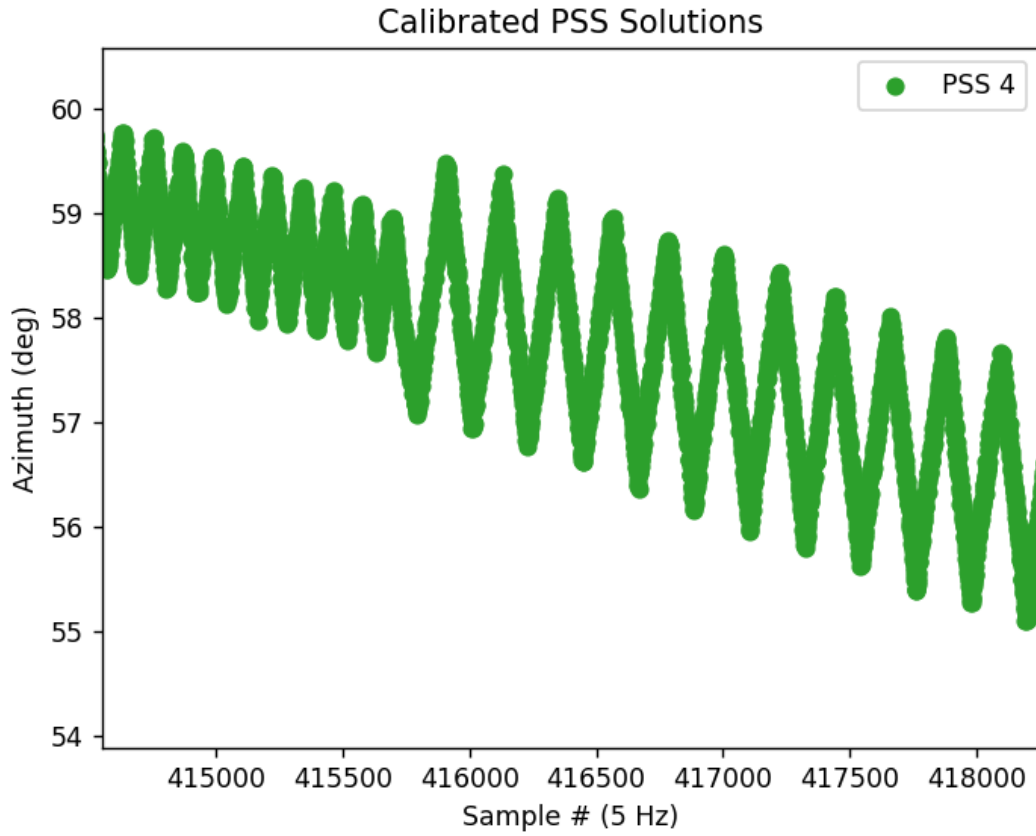


Figure 3.4. The calibrated azimuth solution for PSS4 during a scan of a target. As discussed in Section 2.3, during most target scans we scan slowly in elevation while scanning more quickly in azimuth, which can be seen in this figure.

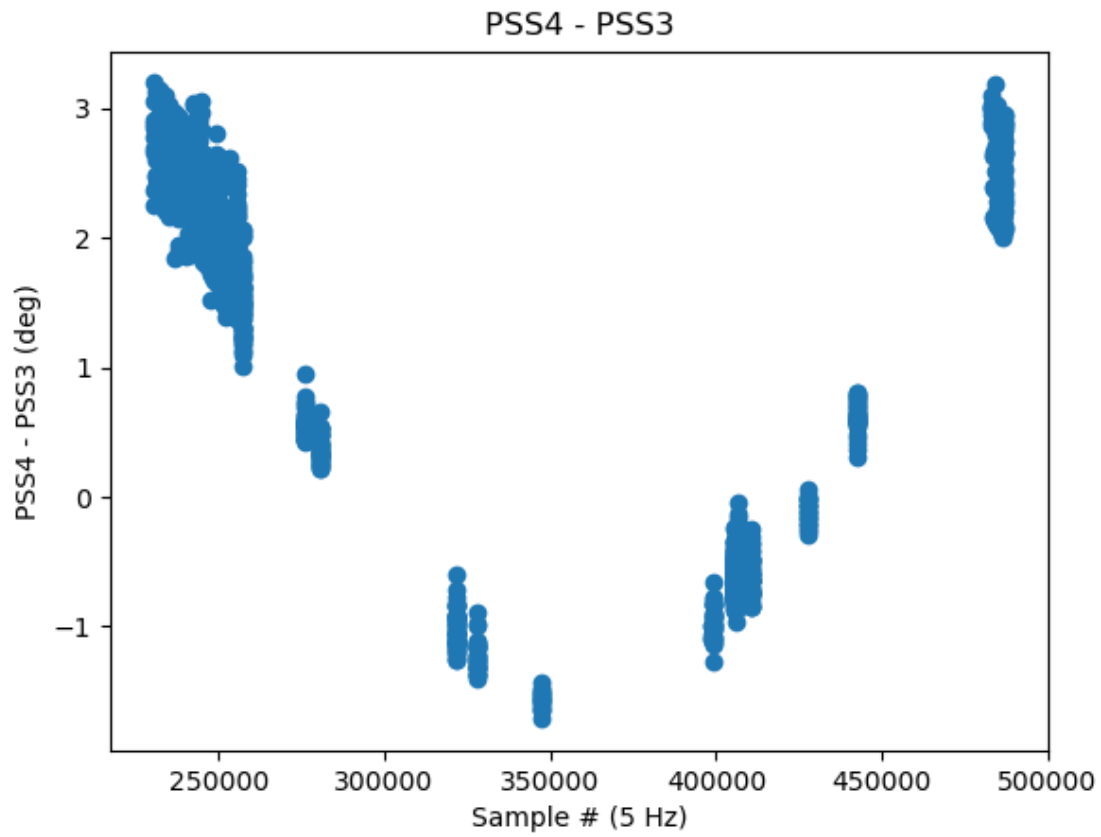


Figure 3.5. Differences between the calibrated azimuth solutions for PSS4 and PSS3, during times when the sun was in the fields-of-view of both sun sensors.

3.3. Finding Home

The coarse pointing sensors have several roles to play both during and after the flight. Their primary role during the flight is to provide corrections to the gyroscope drifts. These drifts can result in absolute pointing errors of order 1° , if no star camera solutions are found for at least an hour. However, using the coarse pointing sensors, most of which obtain pointing solutions continuously, we can calculate the gyroscope drifts and correct for them. Unfortunately, the 2020 flight of BLAST-TNG was short enough that we did not have time to calculate gyroscope drifts and therefore we could not use those for our pointing.

Post-flight, one role the coarse pointing sensors can play is to provide a pointing solution during time periods that the star cameras were unable to obtain solutions. This is especially useful for this flight, in which we had so much contamination from polar mesospheric clouds (PMCs) that the star cameras were often unable to solve the images they took. In this case, we were able to use the calibrated DGPS to improve our pointing solution to better than 1° . This enabled us to determine which object we observed during calibration scans. During our flight planning, we chose several targets that are bright, point-like objects in the sub-mm to use as calibrators. We had observations of these sources from other instruments such as *Herschel*, *Planck*, and LABOCA. One of these sources we named “Home” because it was a source we anticipated being able to observe often. A map of “Home” and several sources around it is shown in Figure 3.6. We originally planned to map only Home, but after the flight when we realized our pointing solution was inaccurate due to the PMCs, we realized that we may have been scanning

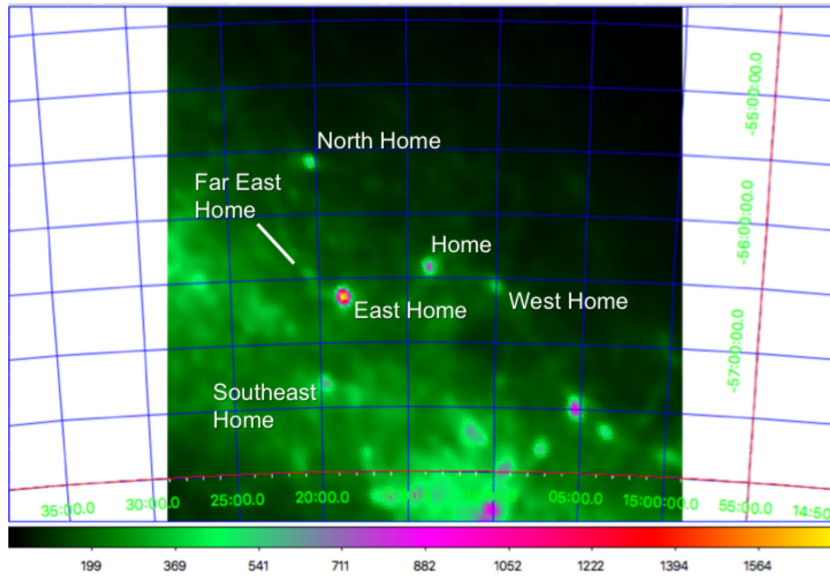


Figure 3.6. A *Planck* 350 μm map of the “Home” source and several sources around it. The colorscale shows specific intensity in units of MJy/sr and the coordinate grid is in right ascension (or RA, horizontal) and declination (or Dec, vertical).

another target, so we gave the other point-like sources in this map names based on their locations relative to Home.

Due to PMCs in the star camera fields-of-view, we were unable to obtain star camera solutions while we observed Home, so our pointing solution was based on star camera solutions from images taken before the scan of Home and extrapolated with the gyroscope measurements. However, due to the gyroscope drifts discussed in Section 2.2, and because there were no star camera solutions for about two hours, these solutions had large errors. Instead, we used the DGPS Azimuth solution with the calibration described in Section

Scan	cross-El pointing error	El pointing error
1	0.570°	0.756°
2	0.557°	0.766°
3	0.625°	0.772°
4	0.500°	0.770°
Average	$0.56 \pm 0.02^\circ$	$-0.766 \pm 0.003^\circ$

Table 3.2. The star camera pointing offsets found from comparing our maps of East Home to those from *Herschel*.

3.1, and we were able to reconstruct our pointing during the scans of Home. From this information, we calculated pointing errors in cross-elevation and elevation, which are listed in Table 3.2 by each scan we made of the East Home region.

We found that we had made a map of East Home, which is shown in Figure 3.7. Comparing this to the *Herschel* map in Figure 3.8, some of the same structures can be identified, including the fainter source to the northeast, which is connected to East Home by a line in both maps. These lines (which were drawn by eye) have position angles within 5° of each other and are exactly the same length. To avoid any residual pointing inaccuracies, we took a single time-stream segment from one detector and compared this to the *Herschel* profile through the source. This is shown in Figure 3.9. The noise level appears higher in the BLAST-TNG data because they are from a single-detector time-stream, while the *Herschel* slices are from co-added maps, using data from all *Herschel* detectors and the entire mission. After identifying the source, we also found that it had been named previously as RCW 92B, an HII region. Identifying which source we observed was not merely a demonstration of the pointing reconstruction we could achieve. This identification allows us to calculate the sensitivity of our detectors to astronomical sources, and this work is ongoing.

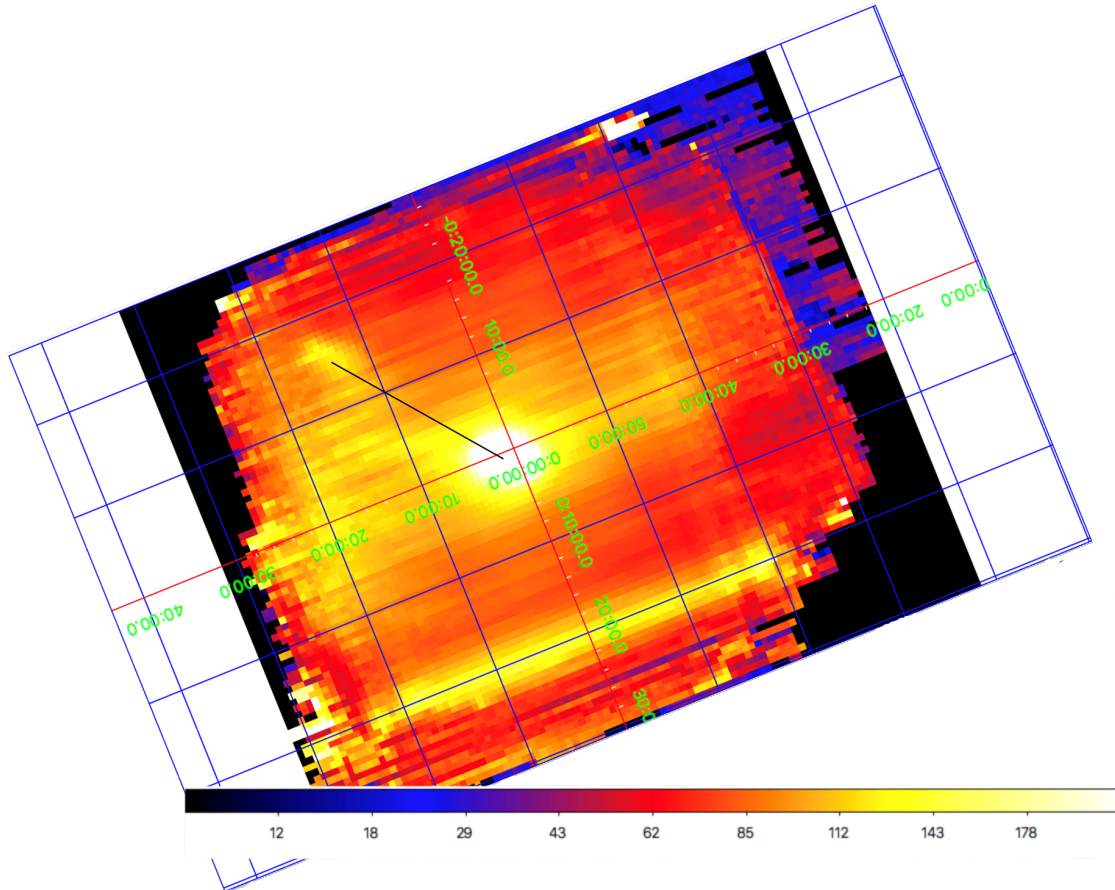


Figure 3.7. BLAST-TNG single detector map of East Home (RCW 92B) with a black line drawn between the two compact sources. The linear object at the bottom of the map is an artifact of the map-making process. The color scale is in instrument units and the coordinates shown are elevation and cross-elevation. The map has been rotated by the parallactic angle of the observation so that North (positive Dec) is up, the same as in the *Herschel* map in Figure 3.8.

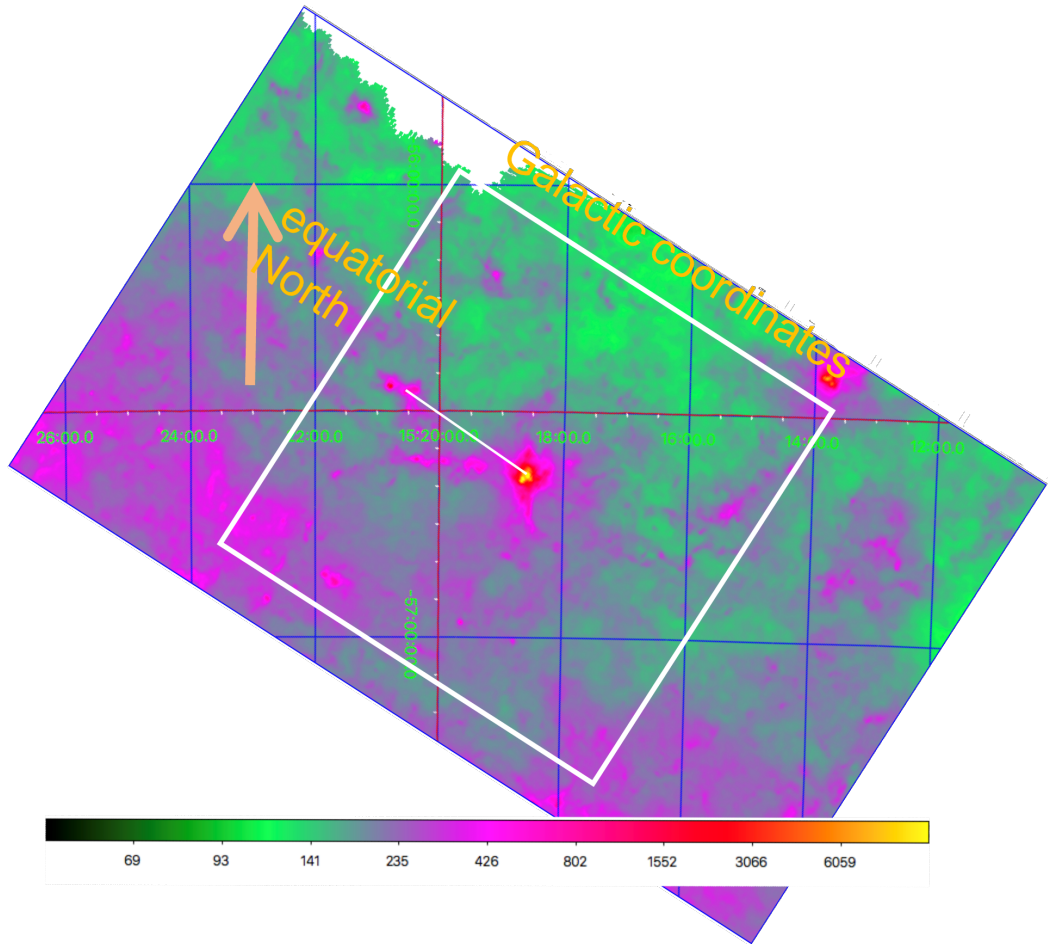


Figure 3.8. *Herschel* co-added map of East Home (RCW 92B) with a white line drawn between the two compact sources. The colorscale is in MJy/sr and the coordinate grid shown is in equatorial coordinates, with RA horizontal and Dec vertical.

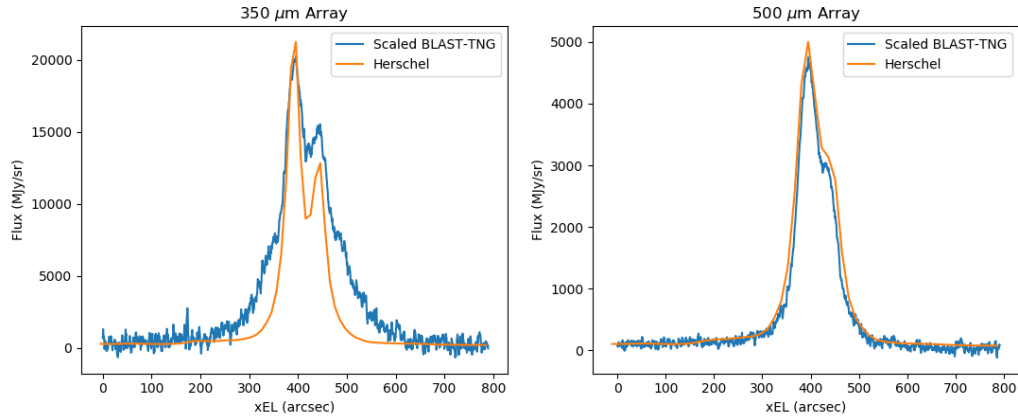


Figure 3.9. Slices through the BLAST-TNG and *Herschel* maps in Figure 3.7 and 3.8 in both the 350 μm and 500 μm bands. The units of the y-axis are from the *Herschel* map, while the BLAST-TNG data have been scaled so the peaks match. The BLAST-TNG data have more noise because they are taken from the time-stream of a single detector, while the *Herschel* data slice was taken through the final co-added map of the source.

CHAPTER 4

PolKa Data Analysis

To compare the large- and small-scale magnetic field in Vela C South Ridge requires multiple instruments whose sensitivities to different angular scales overlap. BLASTPol is sensitive to scales up to a few degrees, and has an angular resolution of $2.5'$ (Fissel et al., 2016). ALMA is sensitive from the size of the primary beam, which is $38.3''$, to the size of the synthesized beam, which has a half-power beam width (HPBW) of $2''$. These two sets of scales do not overlap, so scales would be missing if these were the only data we used to characterize the magnetic field in this source. To fully link the BLASTPol and ALMA data sets, we used data from PolKa, the Polarimeter für bolometer Kameras (English: Polarimeter for bolometer cameras) (Wiesemeyer et al., 2014), instrument on the APEX telescope. APEX, the Atacama Pathfinder Experiment (Güsten et al., 2006), is a 12 m submillimeter telescope on the Chajnantor Plateau in Chile, which is also home to ALMA. PolKa is designed to work with multiple bolometer cameras and enables them to make polarimetric measurements. When used with LABOCA (The Large APEX BOLometer CAmera, Siringo et al. (2009)), a 295-pixel 870 micron submillimeter camera used at APEX, PolKa allows polarization measurements that are sensitive to scales from $2.5'$ to $18''$. This range of scales makes it possible to link BLASTPol and ALMA magnetic field measurements, as can be seen in Figure 1.5.

When we received the PolKa data, we decided to check the results more thoroughly because it is an instrument with few published results, and polarization data analysis is

challenging. We quickly noticed issues with the data. We knew that data close to the edge of the map was not reliable, but nearer the center of the map (but off of our source) there were map areas where the inferred field direction changed discontinuously by about 90° (see Figure 4.1). In polarization data, this is the largest difference there can be between two data points because there is always a 180° ambiguity in the direction of polarization data. A 90° flip in polarization direction is equivalent to a sign flip in both Q and U (see the explanation of Stokes parameters in Section 1.4, especially Figure 1.6).

We also noticed that when we masked the PolKa polarization maps to show only the data with 3σ polarization detections, parts of the map that remained clearly had data quality issues. For example, the upper-right part of the Q map has a striped pattern that is related to the observing strategy of PolKa. However, these data passed the 3σ cut based on the statistical uncertainties calculated by the PolKa pipeline, see Figure 4.2. After noticing these data quality issues, we decided to run additional tests to characterize the PolKa data so we could determine which data were reliable.

Our first test was to compare PolKa and the $500\ \mu\text{m}$ BLASTPol Q and U maps. Our first result is shown in figures 4.3-4.6. These maps can only be compared qualitatively because they are in different units, with the BLASTPol maps in instrument units¹. The most useful way to compare them is by looking at their signs. While the Stokes U maps agree well, the Stokes Q maps agree less well, primarily in the right side of the map. For figures 4.4 and 4.6, we are plotting BLASTPol Q and U in the PolKa convention. The different conventions for Stokes parameters are defined in equations 4.1-4.6. In the

¹The conversion from instrumental units to physical units is possible, in principle. However, it is not very useful in this specific case because the BLASTPol and PolKa maps are at different wavelengths, so we would still only see qualitative agreement between the maps.

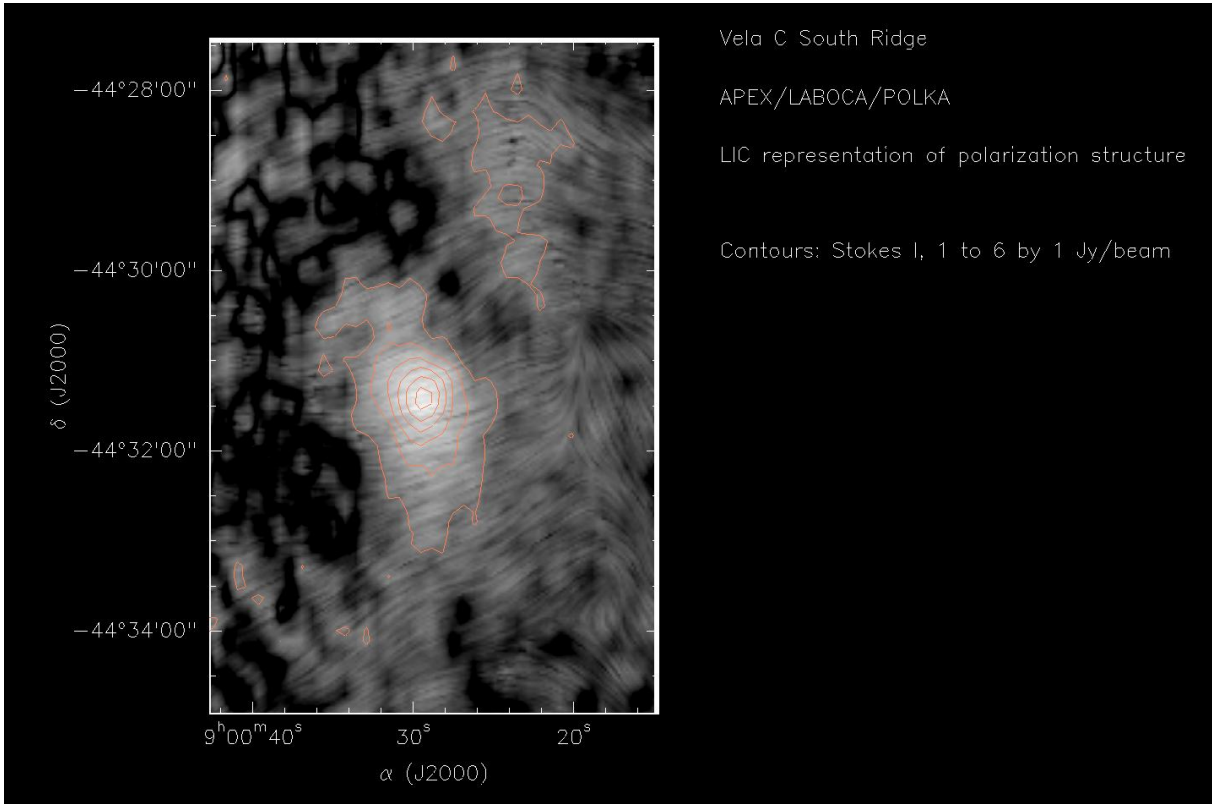


Figure 4.1. PolKa LIC (line integral convolution) map. The background color is PolKa Stokes I (Jy/beam, contours every 1 Jy/beam from 1 to 6 Jy/beam), and the LIC pattern shows the magnetic field direction inferred from polarization. Note the approximately 90° flips in field direction at the center right of the map near $9^{\text{h}}00^{\text{m}}20^{\text{s}}$ R.A. and $-44^\circ31'00''$ to $-44^\circ32'00''$ Dec. This is often an indication of systematic errors in the polarization data.

following, ψ is the angle of the polarization E-vector, defined as zero for a vector oriented north-south, and increasing counter-clockwise (to the east). The BLASTPol data use this convention:

$$(4.1) \quad \psi = 0.5 \arctan(U/Q)$$

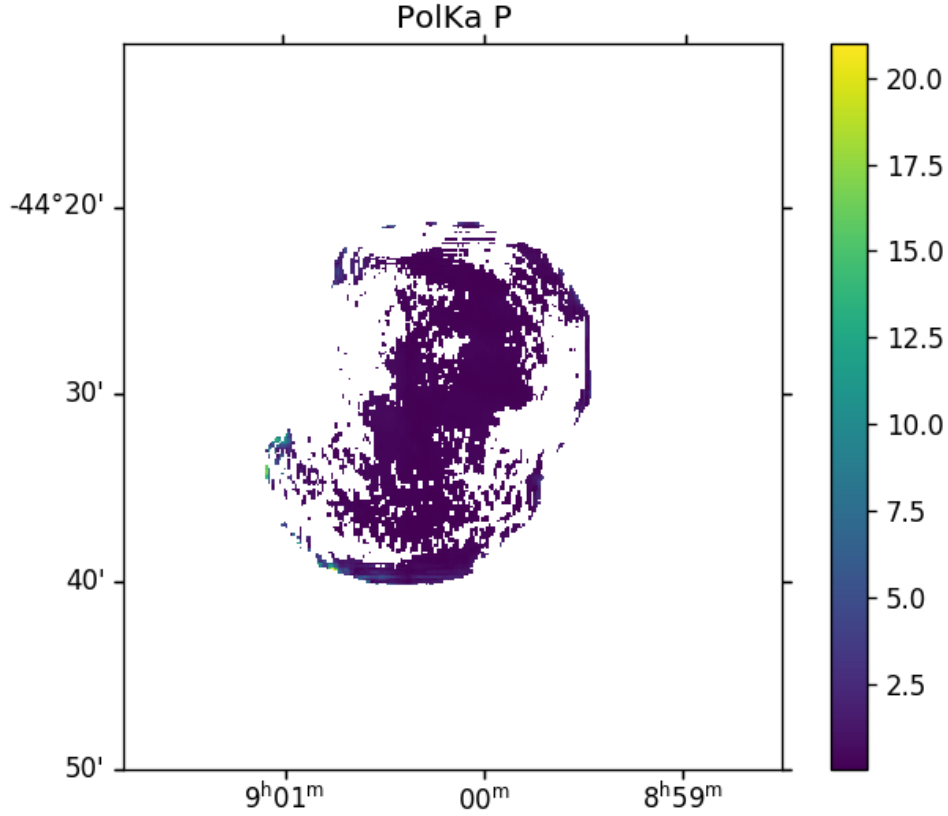


Figure 4.2. PolKa polarized intensity (P) map in Jy/beam, masked to only show 3σ polarization detections, using the statistical uncertainty in P which was provided by the PolKa instrument team. According to this map, we have made 3σ detections of P in many parts of the map, however we know that the edges of the map do not have reliable data because the edges are under-sampled. We also see that the region with 90° polarization flips (as seen in Figure 4.1) has made a significant detection of polarization, according to this figure. This discrepancy convinced us that there were large systematic uncertainties in the PolKa polarization data that were not accounted for in the uncertainties provided by the instrument team.

which is equivalent to:

$$(4.2) \quad Q = P \cos(2\psi)$$

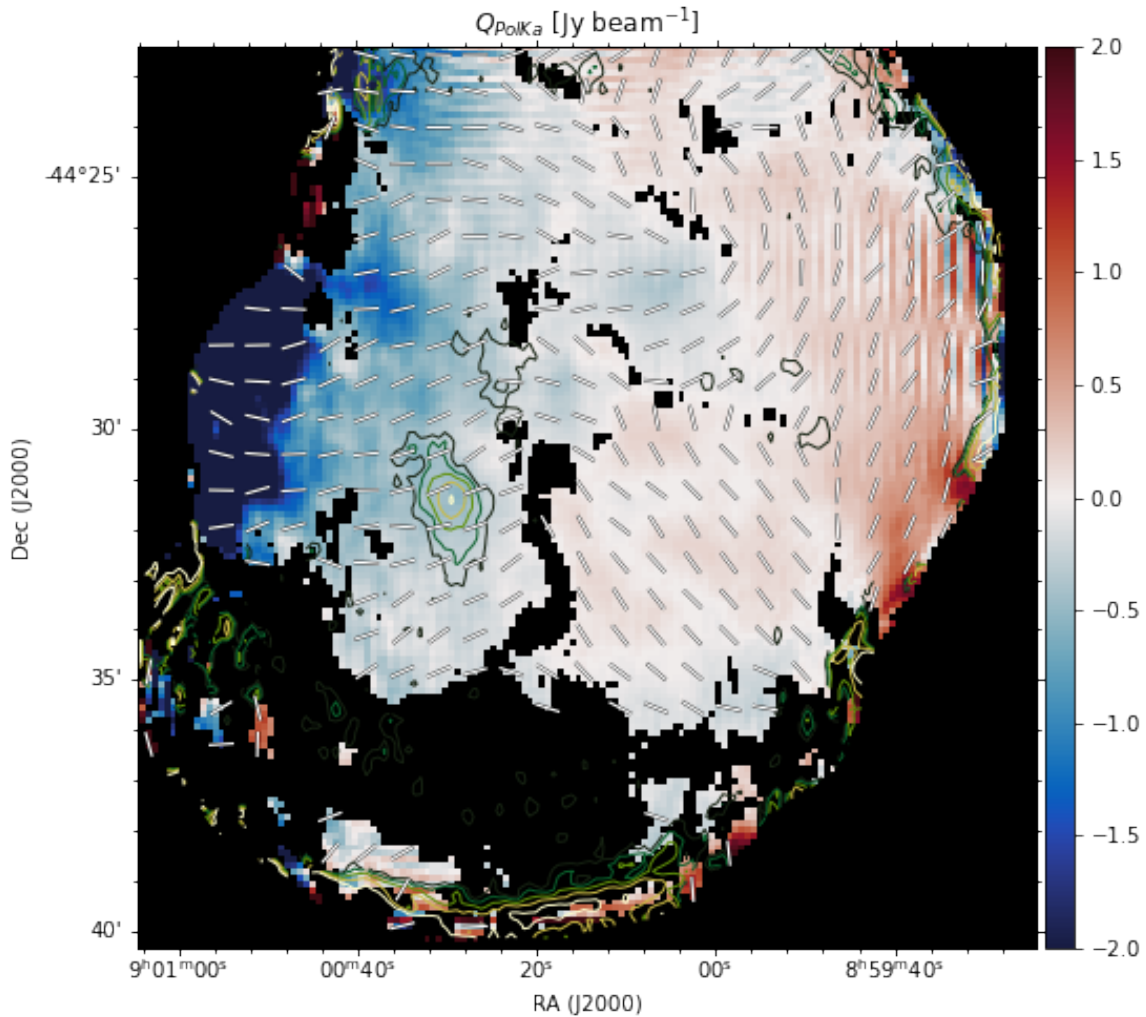


Figure 4.3. PolKa Q map, only showing pixels with 3σ polarized flux detections. The contours show PolKa Stokes I , and the vectors are inferred magnetic field direction from PolKa. Note that this map shows some inconsistencies with the BLASTPol Q map in Figure 4.4, especially on the right side of the map. Note that this Figure uses an early and incorrect version of the mask. The correct map is the one used in Figure 4.2, which mainly differs by more masked data on the right side of the map, and less masked data near the bottom.

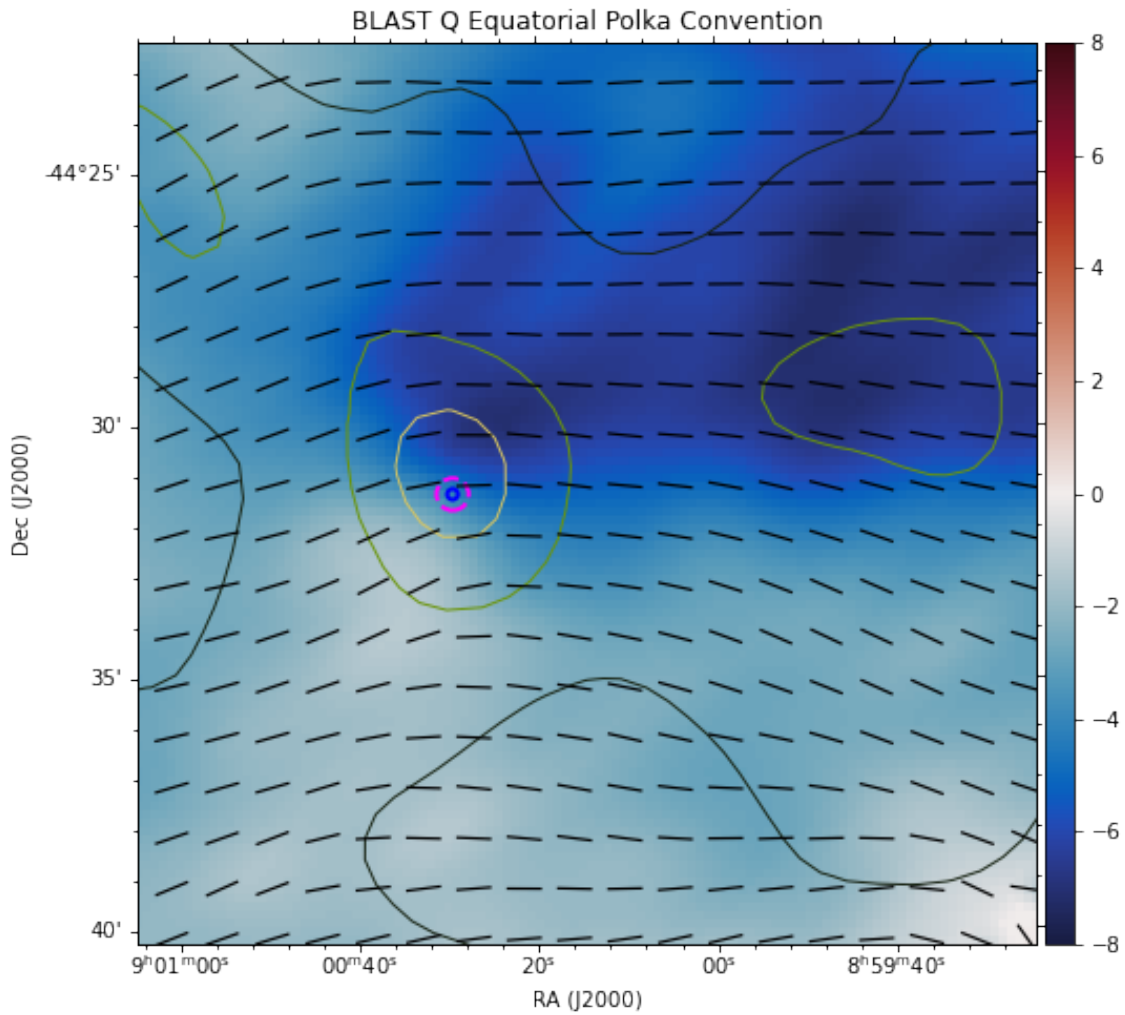


Figure 4.4. BLASTPol Stokes Q map (instrumental units) with contours showing BLASTPol Stokes I and vectors showing BLASTPol inferred field direction. The magenta and blue circles show the ALMA field-of-view and inner 30% of the FOV, respectively. In this map, the sign convention for Q matches the PolKa convention so this map can be directly compared with Figure 4.3.

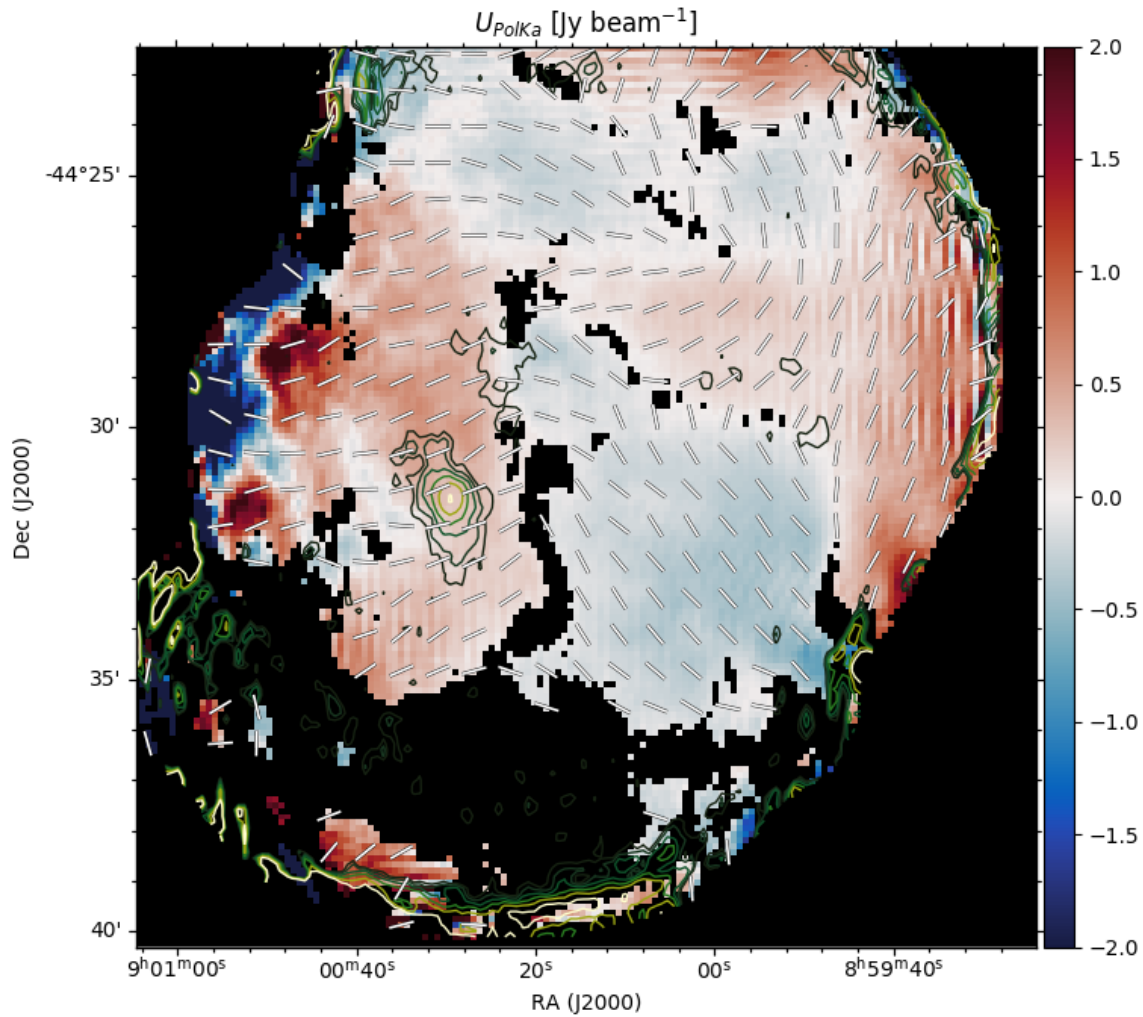


Figure 4.5. Same as 4.3 but with PolKa U instead of Q . Note that this map is largely consistent with the BLASTPol U map shown in Figure 4.6. Especially note the sign of the values, as the units in these maps are not equivalent. Note that this Figure uses an early and incorrect version of the mask. The correct map is the one used in Figure 4.2, which mainly differs by more masked data on the right side of the map, and less masked data near the bottom.

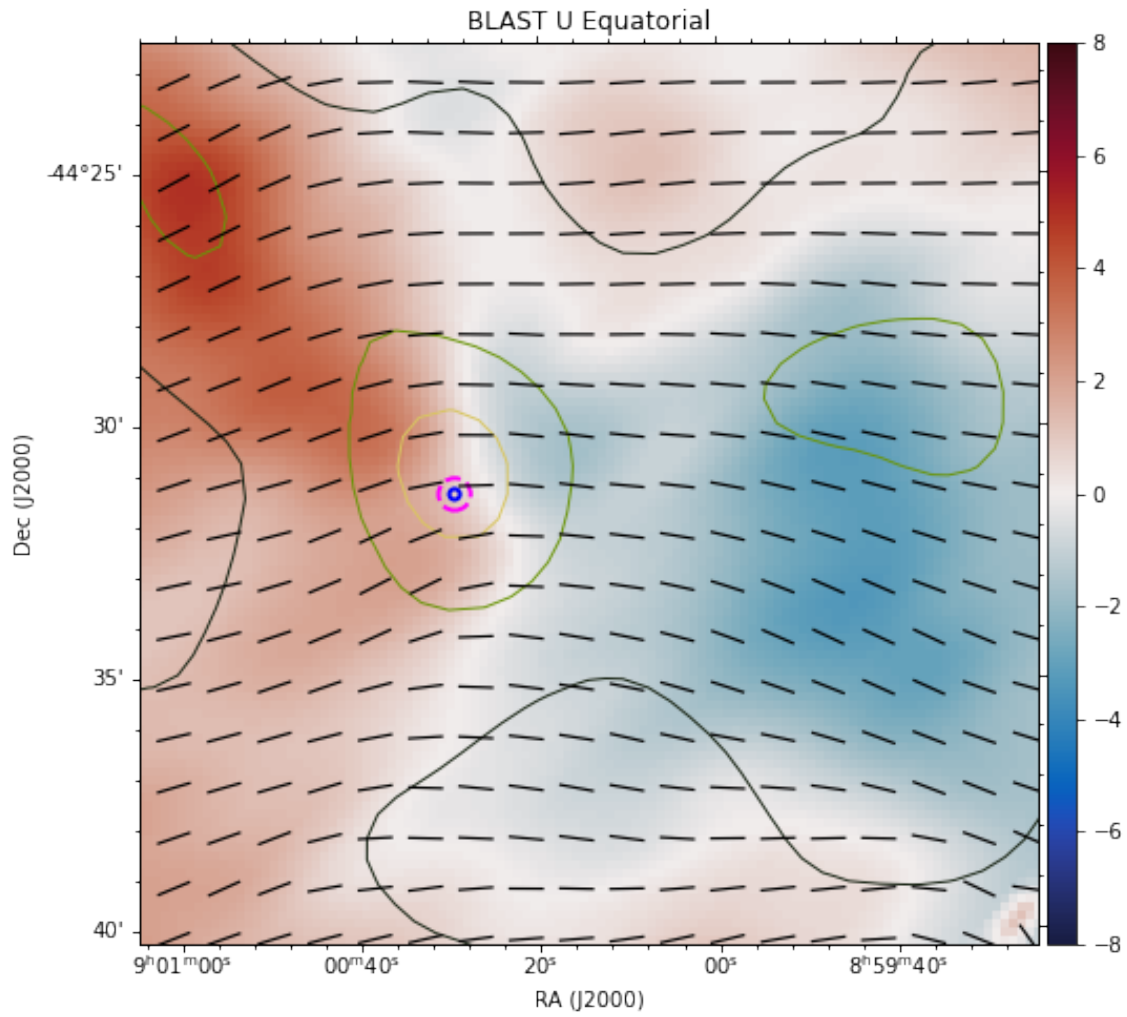


Figure 4.6. BLASTPol Stokes U map (instrumental units) with contours showing BLASTPol Stokes I and vectors showing BLASTPol inferred field direction. The magenta and blue circles show the ALMA field-of-view and inner 30% of the FOV, respectively.

$$(4.3) \quad U = P \sin(2\psi).$$

The PolKa convention is:

$$(4.4) \quad \psi = 0.5[\pi - \arctan(U/Q)]$$

which is equivalent to:

$$(4.5) \quad Q = -P \cos(2\psi)$$

$$(4.6) \quad U = P \sin(2\psi).$$

The final difference being that for the same sky polarization, which we expect both instruments to be measuring, the Q maps have the opposite sign. Therefore, to make our final comparison of BLASTPol and PolKa Stokes maps, we inverted the sign of the BLASTPol Q map.

The results of comparing the BLASTPol and PolKa Stokes maps are seen in Figures 4.5 and 4.6 for the U maps and Figures 4.3 and 4.4 for the Q maps. There are inconsistencies between the two instruments, but in the area of the ALMA target, the two largely agree.

To get a better understanding of the systematic errors in the PolKa data, we next performed jackknife tests on the PolKa data. Jackknife tests involve splitting the data into multiple pieces, analyzing those pieces separately, and comparing the final results. We split the PolKa data by the parallactic angle of the observation. The parallactic angle of the observations varied from 47° to 97° and the median was 79° . This distribution can be seen in Figure 4.7. The parallactic angle ranges we used for the jackknife tests were

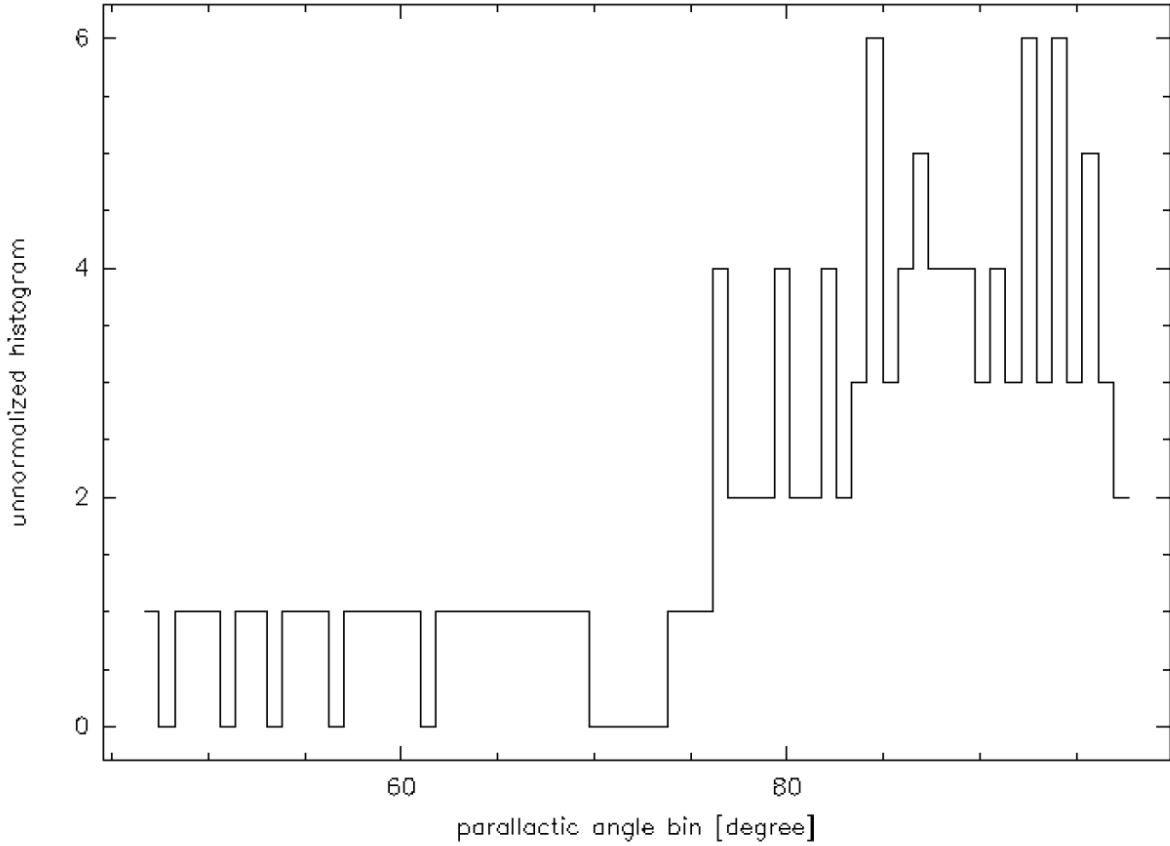


Figure 4.7. Histogram of parallactic angles of the PolKa observations of Vela C South Ridge. The median is 79° , which was used to divide the data into two sets for the jackknife tests.

$[47^\circ, 79^\circ]$ and $[79^\circ, 97^\circ]$. The data for the jackknife tests have the same instrumental polarization correction applied as the full PolKa data set.

For this section on jackknife tests, we will use the usual variables for the Stokes parameters and other measurements we make (I, Q, U, P, p, ψ) but with subscripts 1 and 2 to indicate the two halves of the data. The first set of maps we made for the jackknife tests were a kind of signal-to-noise ratio (SNR) map, where we used the difference between P_1 and P_2 as an estimate for the error on P . We also made the same

kind of maps for Q and U . The most useful of these tests ended up being the SNR map for P because it captures all the behavior of Q and U . Namely, it is not important that a significant detection of Q was not made in a certain map position if U was detected at that position. It is only important whether or not a detection of polarized intensity be made. There is an ambiguity in what to use for the systematic uncertainty found in a jackknife test. One option is, for some quantity X , to use $|X_1 - X_2|$ as the uncertainty, because this is the observed variation. Another option is to use $\frac{|X_1 - X_2|}{2}$, with the argument that $|X_1 - X_2|$ is the difference between the extreme values, so the true value is in the middle, with the uncertainty being half the difference. We decided to use a value halfway in between these, $|X_1 - X_2|/\sqrt{2}$. Therefore, we defined $\text{SNR}(P)$ as:

$$(4.7) \quad \text{SNR}(P) \equiv \sqrt{2} \frac{P}{|P_1 - P_2|}$$

We then implemented a data cut of $\text{SNR}(P) > 2$ for any data we would use for remaining analyses. This so called “ 2σ detection of polarization” is equivalent to a 14° uncertainty in the angle of polarization, and therefore also in the angle of the inferred magnetic field direction. The map of $\text{SNR}(P)$ is shown in Figure 4.8.

We also calculated the angle of polarization using each half of the data set separately. We decided to exclude any data where the difference between the two angles was greater than 20° . Therefore all data used in further analysis had $|\psi_1 - \psi_2| < 20^\circ$.

We made one final cut to the data, this one based on the brightness, or Stokes I , of the map. PolKa is a sensitive instrument in polarization, but in Stokes I , the signal is not modulated, so atmospheric effects are significant. This is what limits the field of view

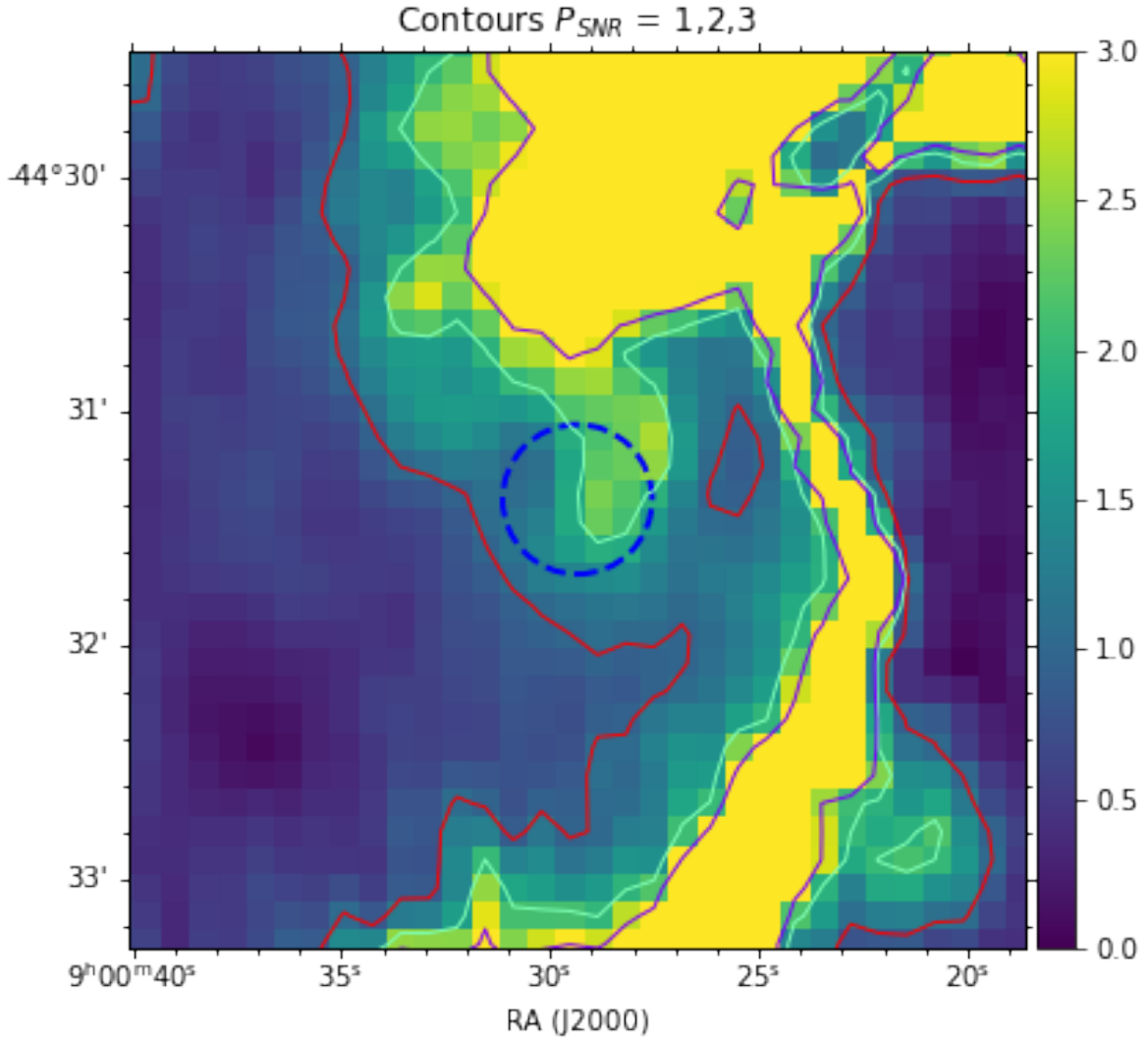


Figure 4.8. $SNR(P)$ as defined in 4.7 shown for the center of the PolKa map. The contours are at $SNR(P) = 1$ (red), 2 (light green), and 3 (purple).

over which Stokes I structure can be recovered to $2.5'$. In order to be conservative, we decided to exclude any data that were not from a relatively bright part of the map. We made a cut at 20% of I_{max} , where I_{max} is the brightest pixel on the target.

To summarize, the cuts we made on the data were:

$$(4.8) \quad \text{SNR}(P) > 2$$

$$(4.9) \quad |\psi_1 - \psi_2| < 20^\circ$$

$$(4.10) \quad I > 0.2I_{max}$$

There are only 41 map pixels that pass all three data cuts, and the boundary of this area is shown by the red contour in Figure 4.9. The pixel scale of this map is $7''$, which is about half the PolKa beam width, so we show one vector per pixel, as in Figure 1.5.

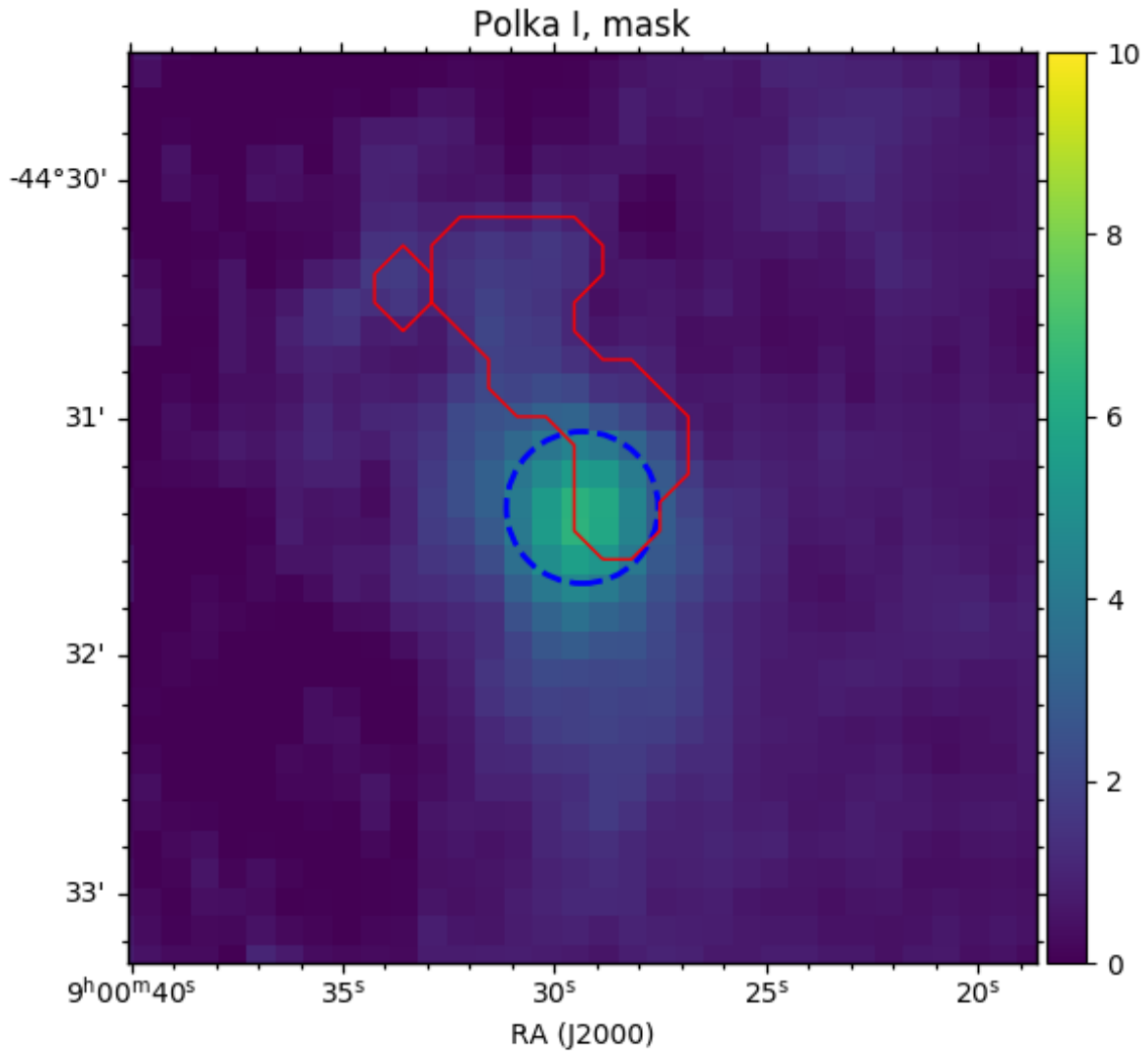


Figure 4.9. The red contour is the boundary of the PolKa mask, plotted over the PolKa Stokes I map (Jy/beam). This is the result of jackknife tests and shows the combination of data cuts as defined in equations 4.8, 4.9, 4.10. The blue dashed circle shows the ALMA field of view.

CHAPTER 5

Magnetic Field Measurements in Vela C South Ridge**5.1. Previous Work**

Vela C is a large, cold giant molecular cloud (GMC) at a distance of 933 ± 94 pc (Fissel et al., 2019). The average temperature of the cloud is 16 K. The low temperature indicates that the cloud is primarily in the early stages of star formation, because as protostellar cores collapse, gravitational potential energy becomes thermal energy, heating the core. Collapsing cores then radiate, which heats the rest of the cloud as well. Figure 5.1 shows a column density model of Vela C made from *Herschel* submillimeter data.

The polarimetry and magnetic field structure in the entire Vela C molecular cloud has been studied in several papers, including Gandilo et al. (2016), Fissel et al. (2016), Santos et al. (2017), Soler et al. (2017), Fissel et al. (2019). For this work, we decided to focus on a small part of Vela C in the South Ridge region, as defined in Hill et al. (2011). South Ridge is a region about 10 pc across, centered at approximately $(l, b) = (265.8, 1.1)$. The boundary of the South Ridge is shown in Figure 5.2. To probe the magnetic field structure at higher resolution than that available from BLASTPol, we used the ALMA and PolKa telescopes. Using these three instruments, we were able to trace the magnetic field structure over 3 orders of magnitude in scale, from 12 pc (the size of South Ridge) to 0.01 pc (the resolution of our ALMA data). Maps from all 3 instruments can be seen in Figure 1.5.

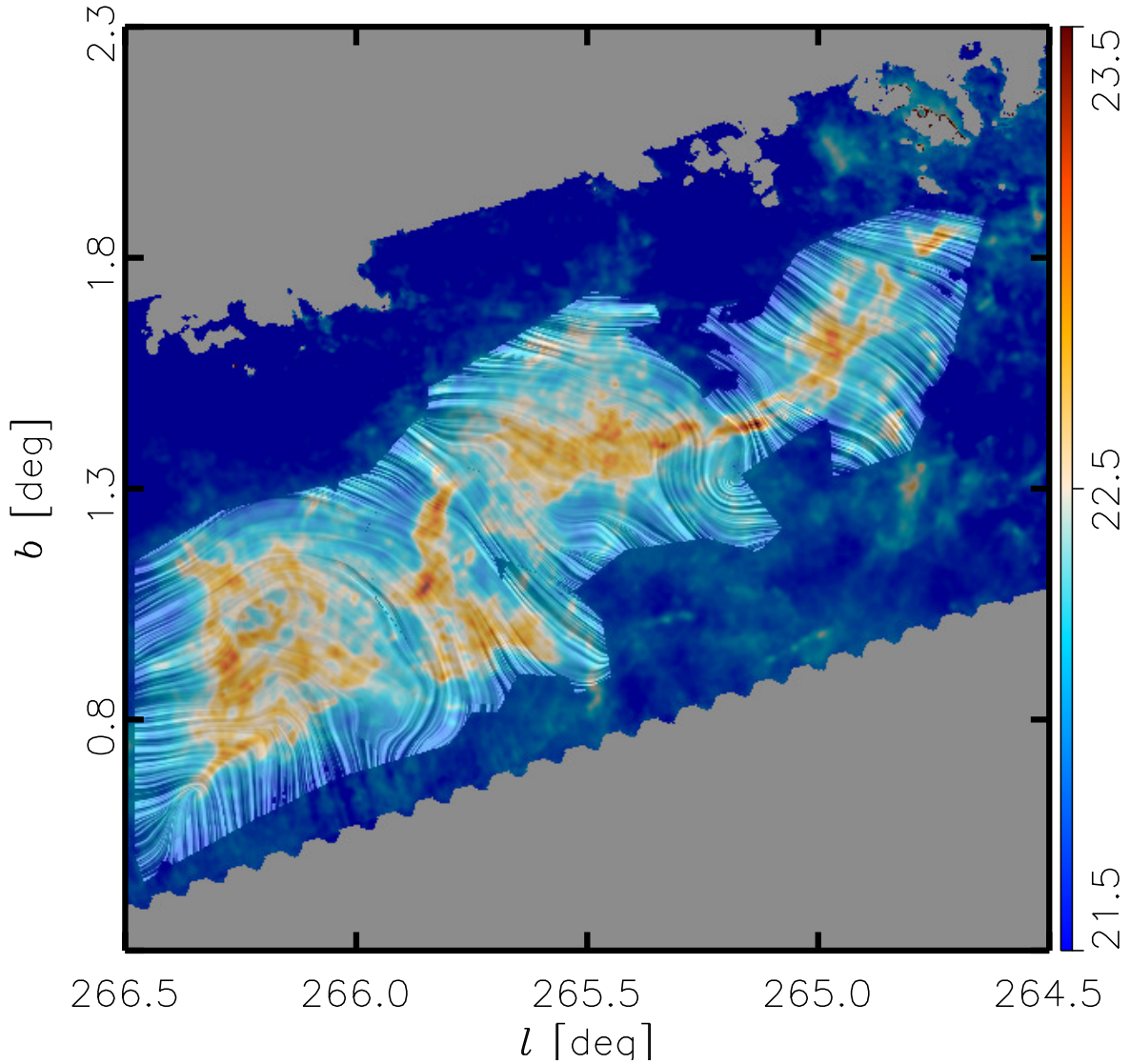


Figure 5.1. *Herschel* column density map of the Vela C Molecular Cloud. The color scale shows the column density in $\log(N_H/1 \text{ cm}^{-2})$. The drapery, or Line Integral Convolution (LIC) pattern shows the direction of the magnetic field inferred from BLASTPol 250 μm polarimetry. South Ridge, which is the target of this work, is the large (about 10 pc across) dense structure centered at approximately $(l, b) = (265.8, 1.1)$. Figure from Soler et al. (2017).

Previous work has shown that magnetic fields are often parallel to filaments in diffuse parts of giant molecular clouds (see references in Planck Collaboration (2016)). Recent work by Planck Collaboration (2016) has shown that in higher column density regions of molecular clouds, a transition occurs and the field is perpendicular to high density filaments. This paper studied just ten nearby molecular clouds. This transition is consistent with a dynamically important magnetic field, as shown by Soler et al. (2013). A dynamically important magnetic field is one that has energy density at least as great as the energy density in turbulent gas motions, that is sub-Alfvénic or trans-Alfvénic. Later work by Soler et al. (2017) showed the same transition in Vela C, which was not included in Planck Collaboration (2016), and the transition was particularly evident in South Ridge.

Our target is the region of South Ridge with the highest column density, which is shown in the bottom panel of Figure 1.5 and the right panel of Figure 5.2. This target is likely an IR-quiet Massive Dense Core (MDC). MDCs are an early stage of high-mass star formation, and often contain at least one high-mass protostar and several protostars with lower masses (Motte et al., 2018). IR-quiet MDCs have low flux at 20 μm compared to the sub-millimeter emission. Integrating the ammonia map in Figure 5.2, the mass of this MDC can be estimated at $\sim 100 M_{\odot}$. This is on the low end for MDCs, which are typically found at around 150 M_{\odot} . This MDC has a diameter of 0.25 pc, which is slightly larger than the typical 0.1 pc. The mass and size suggest that the most massive star forming in this MDC is likely less massive than the average high-mass star. This star may end up being around the threshold between intermediate- and high-mass stars, which is generally set at 8 M_{\odot} (Motte et al., 2018).

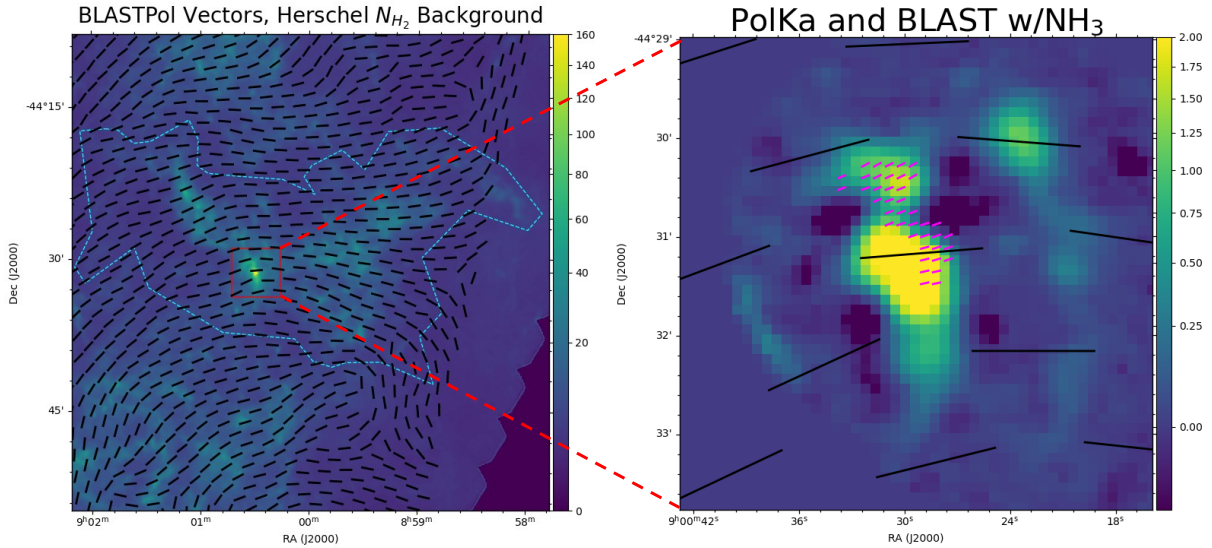


Figure 5.2. South Ridge filamentary structure on multiple scales. The map on the left shows *Herschel* column density (measured in A_V) in the color scale with BLASTPol inferred magnetic field direction shown by the black pseudo-vectors. The dashed blue outline shows the boundary of South Ridge, as defined in Hill et al. (2011). The right panel shows a moment zero ammonia (NH_3) map (Jy/beam km/s) from the hyperfine (1,1) transition at 23.7 GHz, measured by the Australian Telescope Compact Array (ATCA). Ammonia emission traces high column density areas of the cloud. BLASTPol inferred field direction is again shown in black, and PolKa magnetic field direction is shown in magenta.

5.2. Observations

5.2.1. BLASTPol Observations of Vela C

BLASTPol was launched from McMurdo Station, Antarctica on 26 December 2012, local time. During its 12.5 day flight, it observed Vela C for a total of 44 hours, including 43 hours on a “deep” map, with a size of 3.1 deg^2 and 11 hours on a large map, with a size of 10 deg^2 . Both maps covered the region shown in Figure 5.1. BLASTPol observed

simultaneously in three bands centered at 250, 350, and 500 μm . For this work, we used only the maps made at 500 μm .

5.2.2. PolKa Observations of Vela C

PolKa observations of Vela C South Ridge were taken as part of a polarimetry survey of Vela C. The observations of APEX-SR-SMM1 were obtained in December 2011 using the 345 GHz band of LABOCA, which corresponds to 870 μm .

5.2.3. ALMA Observations of Vela C

ALMA observations of the Vela C South Ridge target were executed over 9.3 non-consecutive hours from January 18 to 23, 2019, 6.1 hours of which were observing our target, the remainder was observing calibrators. These observations were conducted using the ALMA 12 m array, using all 43 antennas in configuration C43-1, a compact configuration to maximize the largest recoverable scale (in Stokes I) at $19''$. The maximum recoverable scale of polarization data is $12.6''$, because ALMA polarimetry is restricted to the inner 1/3 of the primary beam. These observations were made in ALMA's Band 4, which has a wavelength coverage of 1.8-2.4 mm.

5.3. Magnetic Field Morphology Across Spatial Scales

In Figure 1.5, we show the magnetic field direction inferred from polarimetry by BLASTPol, PolKa, and ALMA. The three maps cover three orders of magnitude in spatial scale, from the 12 pc size of South Ridge, to the ALMA resolution of 0.01 pc. Comparing the BLASTPol and PolKa vectors in the upper right panel, we see that the field directions are very similar. Likewise, there is similarity between the field directions

measured by PolKa and ALMA as shown in the bottom panel. There is some disorder in the field measured by ALMA, but the measurements nearest the peak of the ALMA Stokes I emission are nearly parallel to the PolKa vectors and the circular mean of the ALMA field directions agrees with the PolKa measurements.

Additionally, Figure 5.2 shows the magnetic field measurements from BLASTPol and PolKa overlaid on maps that show cloud density. The left panel shows BLASTPol vectors on a column density model made with *Herschel*, with the South Ridge region outlined. The main filament in South Ridge, which starts at our target in the red box and goes to the northeast, is perpendicular to the magnetic field as measured by BLASTPol. This same pattern is seen in the right panel, where the elongated structure traced by ammonia emission is perpendicular to the field measured by both BLASTPol and PolKa.

5.4. Magnetic Field Direction Consistency

To quantitatively evaluate the similarity in field direction across the three instruments, we made a box-and-whisker plot showing the distribution of angles measured by each instrument. We also plotted the vectors at the peak of the Stokes I emission as measured by ALMA, where the peak is defined as any pixel where:

$$(5.1) \quad I_{pixel} > \frac{I_{max}}{e}$$

This plot is shown in Figure 5.3. Note that we plotted the box and whiskers for the PolKa measurements in a lighter color because their uncertainty is dominated by systematic rather than statistical errors. The analysis used to find the systematic uncertainty in the

PolKa data was discussed in Chapter 4, but recall that we conducted jackknife tests on the polarization data and all the PolKa measurements used to make Figure 5.3 (and to make Figures 1.5 and 5.2) are 2σ detections of polarization. While we plotted vectors separated by half a beam-width in maps of inferred field direction, for the box plot we used the measurements from every pixel of the map, so not every point is independent. Finally, we plotted one point showing the inferred field direction measurement from BLASTPol, from a polarization map with $10''$ pixels. This shows that the closest BLASTPol measurement to the ALMA source is consistent with field direction measured by ALMA. The orange lines in the box plot represent the circular mean of each set of measurements, rather than the median as is typical. We used the circular mean because it is better suited to angular data than the median.

Given that the PolKa polarization detections are at the 2σ confidence level, the uncertainty on the polarization angle data is 14° . Therefore, all the circular means in Figure 5.3 are consistent with the circular mean of the PolKa measurements. This shows that the magnetic field direction is consistent across three orders of magnitude in spatial scale, from 12 pc to 0.016 pc.

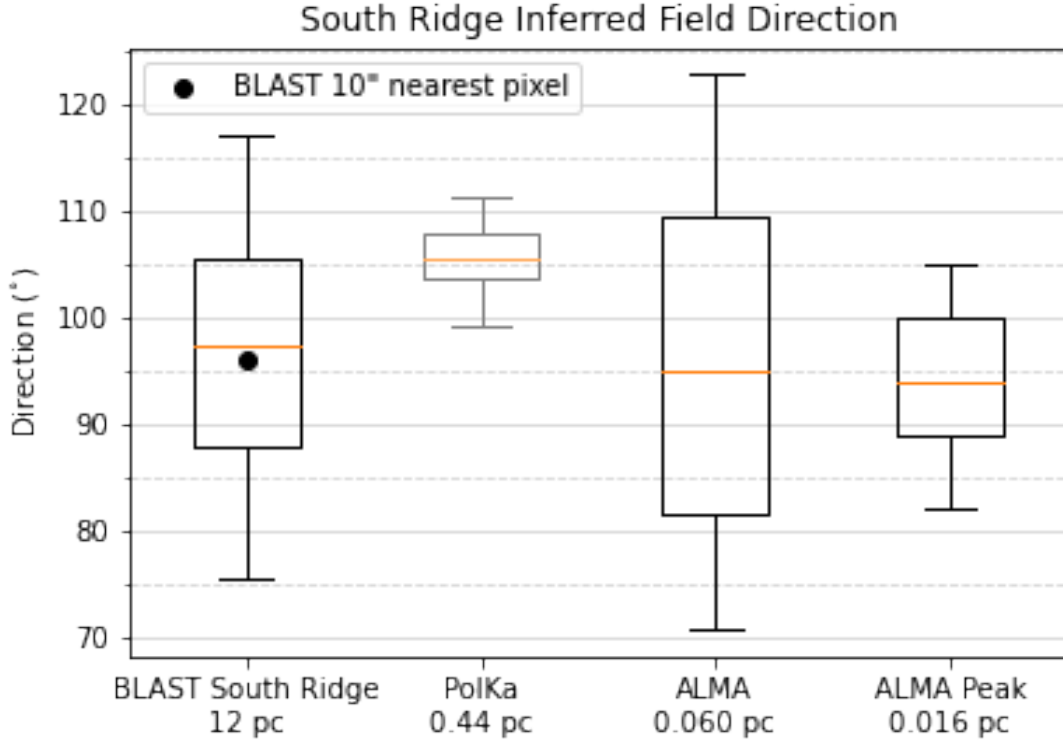


Figure 5.3. Box-and-whisker plot of the distribution (not uncertainty) of inferred magnetic field direction measurements from BLASTPol, PolKa and ALMA polarimetry. The difference between uncertainty and distribution is especially important to note for the PolKa data, which have a very narrow distribution, but a large uncertainty. The PolKa box and whiskers are shown in gray rather than black because this large uncertainty is based on the estimated systematic errors, as discussed in Chapter 4. For all data sets except “ALMA Peak,” all the vectors passing quality cuts from each instrument were included. For “ALMA Peak,” only the vectors within a contour at the I_{max}/e level were included. The orange lines show the circular mean of the angular data, not the median as is typical with box-and-whisker plots.

5.5. Discussion

The results from Sections 5.3 and 5.4 indicate that the magnetic field in the Vela C South Ridge is dynamically important, meaning it is of a comparable strength to

gravitational and turbulent forces. In Sections 5.3 and 5.4, the consistency of the magnetic field direction across scales is discussed. The box-and-whisker plot in Figure 5.3 shows the distributions of the magnetic field directions measured at each scale, and they are all overlapping. This can also be seen by eye in Figure 1.5. In Hull et al. (2017) and Ostriker et al. (2001), the authors showed that a magnetic field direction that is consistent across several orders of magnitude in scale is a signature of a dynamically important magnetic field.

Additionally, Figure 5.2 shows the perpendicularity of the magnetic field to the filamentary structure at two scales. This is the effect seen in the high-column density regime of Histogram of Relative Orientation (HRO) analyses, such as those in Planck Collaboration (2016) and Soler et al. (2017). Due to the similarities between our result and those in papers with detailed HRO analyses, this is additional evidence that the magnetic field is dynamically important in the South Ridge of Vela C on the scales measured by BLASTPol and PolKa. This is in agreement with Soler et al. (2017), who found an HRO signature consistent with a dynamically important magnetic field in South Ridge when comparing *Herschel* with BLASTPol.

The available evidence indicates that our source is an IR-quiet Massive Dense Core, likely forming one or more high- or intermediate-mass stars. The polarimetry from BLASTPol, PolKa, and ALMA, together with a column density model and a map of ammonia emission tracing high volume densities, are all consistent with a dynamically important magnetic field across three orders of magnitude in spatial scale, from 12 pc to 0.01 pc. However, this does not definitively answer the question of the role of magnetic fields in star formation. We know that on some scale, gravity will be stronger than all

other forces, but the question remains: on what scale does that happen? This is a difficult question to fully answer, not least because of the spatial resolution required, which is only available in ALMA observations. In addition, this is not the first time ALMA polarimetry has been used to constrain magnetic field strength in a star forming region: for example, see Hull et al. (2017), who found that the magnetic field in the protostar Serpens SMM1 was consistent with trans-Alfvénic or super-Alfvénic turbulence. Therefore we must consider this question open until more data are available. We discuss the prospects for future observatories in Chapter 6.

CHAPTER 6

Conclusion

6.1. Importance of Star Formation

As we noted in the introduction, star formation is fundamental to astronomy, because all other aspects of the field, from galaxy evolution to planet formation, rely on how stars form. One of the most significant open questions is about the role of magnetic fields in star formation. We know magnetic fields are important, but what is their strength relative to the forces of gravity and turbulence across orders of magnitude in spatial scale? And what sets the star formation efficiency and initial mass function of stars? This work begins to answer these questions with a combination of new instruments and new approaches to observation and data analysis.

6.2. BLAST-TNG

BLAST-TNG is a revolutionary new instrument, capable of mapping dozens of molecular clouds in a single balloon flight. The combination of large primary mirror size, thousands of detectors, and long hold-time cryostat all served to make it a powerful telescope for mapping magnetic fields in star forming regions. The large mirror required advances in optical technology due to the weight limits imposed by the ballooning platform. We manufactured the primary mirror, optics bench, and struts for the secondary from carbon fiber. The optical surface of the primary was then coated in aluminum to increase the reflectivity in the submillimeter.

We achieved an order of magnitude increase in detector number (from 270 to 3318) by using MKIDs, which were multiplexed by up to a factor of ~ 600 so that we only required five readout cables. This vastly simplified the receiver design as well as improved the hold-time of the cryostat by reducing the total thermal loading. Other improvements to the cryostat resulted in a hold-time of approximately 24 days. All of these improvements increased our sensitivity and our maximum flight time, which would have enabled us to make up to eight times as many independent measurements of magnetic field direction as BLASTPol did, and at higher resolution. However, because our flight was cut short after only 15 hours, we did not make any observations of our science targets.

Our flight was a success from a technical standpoint. We demonstrated that our cryogenic receiver and detectors worked in-flight, and become the first instrument to operate a kilo-pixel array of MKIDs from above the ground. As discussed in Chapter 3, we were able to reconstruct our pointing, which allowed us to demonstrate the sensitivity of the MKIDs in-flight.

6.3. Vela C South Ridge Magnetic Field Measurements

Although BLAST-TNG did not observe any of our scientific targets, we were able to make progress on our scientific goals by acquiring ALMA and PolKa data for Vela C, a molecular cloud mapped by BLASTPol in 2012. We compared the magnetic field measurements made by these three instruments, which spanned three orders of magnitude in spatial scale, and found that the magnetic field direction was unchanged across all scales. We also found that the magnetic field directions in these data were perpendicular to dense structures, as measured by a *Herschel* column density model and ammonia

emission measured by ATCA. The consistency of the field direction across scales together with the perpendicularity of fields to dense structures is consistent with star formation simulations with strong magnetic fields—that is, fields having energy density at least equal to the energy density of turbulent gas motions. Although tracing magnetic field direction across scales is a relatively new approach, it has been attempted several times before. In Li et al. (2015), the authors found the same consistency across scales as we did. However, in Hull et al. (2017), the authors found that the magnetic field morphology in Serpens SMM1 was consistent with either super-Alfvénic or trans-Alfvénic turbulence, that is either a weak magnetic field or a field equally as strong as turbulence. Our result and Li et al. (2015) are in tension with Hull et al. (2017), therefore more work is needed. To fully constrain the role of magnetic fields in star formation will require many more analyses of this type.

6.4. Future Work

In the coming years, new instruments will continue to explore the role of magnetic fields in star formation. One of these in particular is BLAST Observatory (the Balloon-borne Large Aperture Submillimeter Telescope Observatory). BLAST Observatory is the next iteration in the BLAST saga, and will continue the mission of BLAST-TNG with a new design. BLAST Observatory is designed to fly on a super pressure balloon, which is capable of flights of up to 100 days. To fly on this type of balloon will require a reduction in the total instrument weight by about half. The BLAST team will achieve this by reducing the size of the primary mirror, and shifting one observing band to higher frequencies to retain high angular resolution. We have designed BLAST Observatory with

a monocoque shell, which reduces weight while remaining sufficiently rigid and strong to support the instrument. A reduced power budget will be achieved by switching to a new generation FPGA readout system, that will read out 8274 detectors and use about 1/10 the power of the BLAST-TNG readout system.

BLAST Observatory will map several nearby molecular clouds at high spatial resolution, and dozens of more distant clouds. It will have the necessary angular resolution and sensitivity to large angular scales to directly link ALMA and *Planck* magnetic field measurements, without the need for intermediate instruments like PolKa, as were used in this work. BLAST Observatory will also be capable of constraining dust composition models and measuring the properties of turbulence in the ISM.

In addition to BLAST Observatory, ongoing improvements to ALMA will increase its ability to answer questions about star formation. For example, polarimetry with the Atacama Compact Array and mosaicing of polarimetric observations will both increase the largest recoverable scales of ALMA polarization data. This will allow ALMA observations to cover a larger range of spatial scales, which will help answer the question of the role of magnetic fields in star formation, among many others.

References

- Austermann, J. E., Beall, J. A., Bryan, S. A., et al. 2018, ArXiv e-prints, arXiv:1803.03280
- Brown, R. L., Wild, W., & Cunningham, C. 2004, *Advances in Space Research*, 34, 555
- Chapman, D., Didier, J., Hanany, S., et al. 2014, in *Proc. SPIE*, Vol. 9152, *Software and Cyberinfrastructure for Astronomy III*, 915212
- Crutcher, R. M. 2012, *ARA&A*, 50, 29
- Day, P. K., LeDuc, H. G., Mazin, B. A., Vayonakis, A., & Zmuidzinas, J. 2003, *Nature*, 425, 817 EP . <http://dx.doi.org/10.1038/nature02037>
- Devlin, M. J., Ade, P. A. R., Aretxaga, I., et al. 2009, *Nature*, 458, 737
- Dober, B., Austermann, J. A., Beall, J. A., et al. 2016, *Journal of Low Temperature Physics*, 184, 173
- Fissel, L. M., Ade, P. A. R., Angilè, F. E., et al. 2016, *ApJ*, 824, 134
- Fissel, L. M., Ade, P. A. R., Angilè, F. E., et al. 2019, *The Astrophysical Journal*, 878, 110. <http://dx.doi.org/10.3847/1538-4357/ab1eb0>
- Galitzki, N., Ade, P. A. R., Angilè, F. E., et al. 2014, *Ground-based and Airborne Telescopes V*, doi:10.1117/12.2054759. <http://dx.doi.org/10.1117/12.2054759>
- Galitzki, N., Ade, P., Angilè, F. E., et al. 2016, in *Proc. SPIE*, Vol. 9914, *Millimeter, Submillimeter, and Far-Infrared Detectors and Instrumentation for Astronomy VIII*, 99140J
- Gandilo, N. N., Ade, P. A. R., Angilè, F. E., et al. 2016, *ApJ*, 824, 84

- Geach, C., Hanany, S., Fritts, D. C., et al. 2020, *Journal of Geophysical Research (Atmospheres)*, 125, e33038
- Güsten, R., Nyman, L. Å., Schilke, P., et al. 2006, *A&A*, 454, L13
- Hill, T., Motte, F., Didelon, P., et al. 2011, *A&A*, 533, A94
- Hoang, T., & Lazarian, A. 2008, *MNRAS*, 388, 117
- Hull, C. L. H., Girart, J. M., Tychoniec, L., et al. 2017, *ApJ*, 847, 92
- Kjellstrand, C. B., Jones, G., Geach, C., et al. 2020, *Earth and Space Science*, 7, 01238
- Korotkov, A. L., English, M.-P., Tucker, G. S., Pascale, E., & Gandilo, N. 2013, *Journal of Astronomical Instrumentation*, 2, 1350005
- Krumholz, M. R., & Federrath, C. 2019, *Frontiers in Astronomy and Space Sciences*, 6, 7
- Lamarre, J. M., Puget, J. L., Ade, P. A. R., et al. 2010, *A&A*, 520, A9
- Lang, D., Hogg, D. W., Mierle, K., Blanton, M., & Roweis, S. 2010, *The Astronomical Journal*, 139, 1782–1800. <http://dx.doi.org/10.1088/0004-6256/139/5/1782>
- Li, H. B., Goodman, A., Sridharan, T. K., et al. 2014, in *Protostars and Planets VI*, ed. H. Beuther, R. S. Klessen, C. P. Dullemond, & T. Henning, 101
- Li, H.-B., Yuen, K. H., Otto, F., et al. 2015, *Nature*, 520, 518
- Lourie, N. P., Angilè, F. E., Ashton, P., et al. 2018a, in *Ground-based and Airborne Telescopes VII*, Vol. 10700, *Proc. SPIE*
- Lourie, N. P., Ade, P., Angilè, F. E., et al. 2018b, in *Millimeter, Submillimeter, and Far-Infrared Detectors and Instrumentation for Astronomy IX*, Vol. 10708, *Proc. SPIE*
- Lowe, I., Ade, P. A. R., Ashton, P. C., et al. 2020, in *Society of Photo-Optical Instrumentation Engineers (SPIE) Conference Series*, Vol. 11453, *Society of Photo-Optical Instrumentation Engineers (SPIE) Conference Series*, 1145304

- Marsden, G., Ade, P. A. R., Bock, J. J., et al. 2009, *ApJ*, 707, 1729
- Mauskopf, P. D. 2018, *PASP*, 130, 082001
- McKee, C. F., & Ostriker, E. C. 2007, *ARA&A*, 45, 565
- McKenney, C. M., Austermann, J. E., Beall, J. A., et al. 2019, *Review of Scientific Instruments*, 90, 023908
- Miller, A. D., Fritts, D. C., Chapman, D., et al. 2015, *Geophys. Res. Lett.*, 42, 6058
- Motte, F., Bontemps, S., & Louvet, F. 2018, *ARA&A*, 56, 41
- Ostriker, E. C., Stone, J. M., & Gammie, C. F. 2001, *ApJ*, 546, 980
- Pascale, E., Ade, P. A. R., Bock, J. J., et al. 2009, *ApJ*, 707, 1740
- Planck Collaboration. 2016, *A&A*, 586, A138
- Planck Collaboration, Ade, P. A. R., Aghanim, N., et al. 2014, *A&A*, 571, A6
- . 2015, *A&A*, 576, A104
- Santos, F. P., Ade, P. A. R., Angilè, F. E., et al. 2017, *ApJ*, 837, 161
- Siringo, G., Kreysa, E., Kovács, A., et al. 2009, *A&A*, 497, 945
- Soler, J. D., Hennebelle, P., Martin, P. G., et al. 2013, *ApJ*, 774, 128
- Soler, J. D., Ade, P. A. R., Angilè, F. E., et al. 2017, *A&A*, 603, A64
- Takakura, S., Aguilar-Fafández, M. A. O., Akiba, Y., et al. 2019, *The Astrophysical Journal*, 870, 102. <http://dx.doi.org/10.3847/1538-4357/aaf381>
- Thomas, G. E., & McKay, C. P. 1985, *Planetary and Space Science*, 33, 1209
- Wiesemeyer, H., Hezareh, T., Kreysa, E., et al. 2014, *PASP*, 126, 1027